Global ray tracing simulations of the SABER gravity wave climatology

Peter Preusse,[1] Stephen D. Eckermann,[2] Manfred Ern,[1] Jens Oberheide,[3] Richard H. Picard,[4] Ray Roble,[5] Martin Riese,[1] James M. Russell III ,[6] and Martin G. Mlynczak[7]

Abstract. Since February 2002 the Sounding of the Atmosphere using Broadband Emission Radiometry (SABER) instrument on board the Thermosphere-Ionosphere-Mesosphere Energetics and Dynamics (TIMED) satellite has measured temperatures throughout the entire middle atmosphere. Employing the same techniques as previously used for the Cryogenic Infrared Spectrometers and Telescopes for the Atmosphere (CRISTA), we deduce from SABER data five years of gravity wave (GW) temperature variances from 20 km to 100 km altitude. A typical annual cycle is presented by calculating averages for the individual calendar months. Findings are consistent with previous results from various satellite missions. Based on July data and zonal mean GW momentum flux from CRISTA, a homogeneous and isotropic launch distribution for the Gravity wave Regional Or Global RAy Tracer (GROGRAT) is inferred. The launch distribution contains different phase speed mesoscale waves, some of very high phase speed and extremely low amplitudes, as well as waves with horizontal wavelengths of several thousand kilometers. Global maps for different seasons and altitudes as well as time series of zonal mean GW squared amplitudes based on this launch distribution match the observations well. Based on this realistic observation-tuned model run, we can calculate quantities which cannot be addressed by measurements and which are speculated to be major sources of uncertainty in current generation GW parameterization schemes. Two examples presented in this paper are the average cross-latitude propagation of GWs and the relative acceleration contributions provided by saturation and dissipation, on the one hand, and the horizontal refraction of GWs by horizontal gradients of the mean flow, on the other hand.

1. Introduction

Gravity waves (GWs) are an important dynamical driving force for the middle atmosphere. They are believed to be the main drivers of the mesospheric circulation and the cold summer mesopause [McLandress, 1998], to provide about half of the momentum required for driving the quasi-biennial oscillation (QBO) in the tropics [Dunkerton, 1997], and to contribute significantly to the Brewer-Dobson circulation [Alexander and Rosenlof, 2003]. However, GW parameterizations used in global modeling are strongly simplified. In these schemes GWs are assumed to propagate purely vertically remaining inside the same general circulation model (GCM) grid col-

[1]Institute of Chemistry and Dynamics of the Geosphere, ICG-1: Stratosphere, Research Center Jülich, Juelich, Germany

[2]Space Science Division, Naval Research Laboratory, Washington, DC, USA

[3]Department of Physics, Wuppertal University (BUW),Wuppertal, Germany

[4]Air Force Research Laboratory, Hanscom Air Force Base, Hanscom, MA, USA

[5]High Altitude Observatory, National Center for Atmospheric Research, Boulder, CO, USA

[6]Hampton University, Hampton, VA, USA

[7]NASA Langley Research Center, Hampton, VA, USA

0148-0227/08/$9.00

umn, not to change their horizontal propagation direction and to transfer momentum merely by wave-breaking processes [Hines, 1997; Warner and McIntyre, 1999; Alexander and Dunkerton, 1999; Medvedev and Klaassen, 2000] the latter themselves remaining a source of uncertainty [Chimonas, 1999; Hines, 1999; Fritts and Alexander, 2003; Achatz, 2007]. Furthermore, despite their importance experimental constraints on the global distribution of GWs and their sources still remained poor.

It was first realized by Fetzer and Gille [1994] that satellite instruments can observe gravity waves (GWs) from space. During the last decade the number of instruments with sufficient spatial resolution to resolve GWs has increased. Each type of instrument can detect only a certain part of the vertical and horizontal wave spectrum of GWs. Overviews and comparisons of different observation methods as well as the range of detectable vertical and horizontal wavelengths are given by Wu et al. [2006] and Preusse et al. [2008]. Infrared emission limb sounders have the advantage that they can resolve a wide range of vertical wavelengths. A particular benefit of the SABER data [Mlynczak, 1997; Russel et al., 1999; Yee et al., 2003] is that they cover the entire middle atmosphere and lower thermosphere.

The SABER instrument has now operated for more than five years. This provides the opportunity to search for semi-annual, annual and biennial variations of GW amplitudes [Krebsbach and Preusse, 2007; Ern et al., 2007] and to generate a statistically meaningful climatology of the annual cycle. This distinguishes SABER from previous investigations of infrared limb emissions (e.g. Fetzer and Gille [1994]; Eckermann and Preusse [1999]; Preusse and Ern [2005]; Ern et al. [2006]), which cover a smaller altitude range and discuss (with the exception of the CLAES data; Preusse and Ern [2005]) only selected time slices of one month or less.

The new SABER time series offers more comprehensive test conditions for global GW modeling, and in particular, provides the opportunity to adapt the launch setup of a model according to measured data. Conventionally, global GW modeling starts with a semi-empirical or process-based GW source distribution, propagates the waves through the background wind and temperature fields and compares the results to measured distributions. For instance, Alexander [1998] used a model based on a comprehensive set of single waves with horizontal wavelengths between 6 km and 800 km, periods between 15 minutes and 4 hours, and constant launch momentum flux for all waves, which means a red distribution in wave variance. The results were compared to Microwave Limb Sounder (MLS) [Wu and Waters, 1997] and in-situ measurements [Eckermann et al., 1995; Allen and Vincent, 1995]. Eckermann and Preusse [1999] and Jiang et al. [2004b] used the physically based launch distribution of the Naval Research Laboratory Mountain Wave Forecast Model (NRL-MWFM) and compared GW hindcasts to measurements by the CRyogenic Infrared Spectrometers and Telescopes for the Atmosphere (CRISTA) infrared emission limb sounder and to MLS data, respectively. Though in both cases the measurements were well matched by the model hindcasts, Jiang et al. [2004b] concluded that there were still too many degrees of freedom to infer model improvements or identify model deficiencies. Ern et al. [2006] compared model results from the CRISTA-1 and CRISTA-2 mission with offline simulations using the Warner and McIntyre spectral parameterization scheme [Warner and McIntyre, 1999, 2001]. They were able to confine the ranges of the tunable model parameters, but also found indications that even with the best choice of parameters the model overestimates GW activity at high summer latitudes. A ray tracing simulation consisting of four mid-frequency and three long horizontal wavelength components for August 1997 compared to CRISTA-2 and SABER GW squared amplitudes [Preusse et al., 2006] seems to confirm this finding but covers too small a latitude range to be conclusive.

In this paper we take the opposite approach. We compare the results of single spectral components with the SABER measurements and select components for a composite experiment in such a way that the observed global distributions and their annual cycle are well matched. Although this solution will not be truly unique and some uncertainties will remain, such a measurement-guided GW model setup can be valuable for quantitatively estimating the importance of effects conventionally neglected in GW parameterization schemes, such as oblique wave propagation, refraction of the horizontal wave vector and wave damping by radiative and turbulent processes.

For instance, Bühler and McIntyre [2003] made the point that the horizontal refraction of GWs in horizontal wind shear inside the polar vortex acts at different locations and in a different way than conventional GW schemes based on wave dissipation. Their approach, however, is purely theoretical and therefore cannot quantitatively assess its importance in the real world. Accelerations calculated in this paper will provide a first realistic estimate for this question.

The technique for analyzing SABER data in terms of GWs is briefly discussed in section 2. Section 3 introduces the GROGRAT ray tracer and the background atmosphere prepared for the ray tracing experiments. Section 4 uses SABER zonal mean GW squared amplitudes measured for July as well as CRISTA momentum flux values to determine an "optimal" launch distribution. In section 5, global maps as well as zonal mean cross sections of a typical annual cycle composed from almost five years of SABER data are compared to GROGRAT modeling results. Section 6 uses the GROGRAT model to estimate average cross-latitude propagation and calculates accelerations. A summary and discussion are given in section 7.

2. Instrument and analysis technique

The SABER instrument [Mlynczak, 1997; Russel et al., 1999; Yee et al., 2003] is an infrared emission limb sounder covering the upper troposphere, whole middle atmosphere and lower thermosphere. Temperatures are retrieved from the main CO_2 ν_2 emission at 15 μm. A new coupled retrieval algorithm evaluates CO_2 densities and temperatures simultaneously from 4.3 μm and 15 μm emissions and takes into account non-local thermodynamic equilibrium (NLTE) effects [Mertens et al., 2001, 2004]. NLTE effects and interaction with chemistry start to exert an influence above $\sim$70 km altitude and become increasingly important in the mesopause and lower thermosphere region [Kutepov et al, 2006]. Accordingly, SABER temperature errors are well below 1 K for altitudes below 75 km, about 1.4 K at 80 km and increase above this altitude [Mertens et al., 2001]. The most recent estimate for Version 1.06 data states a preliminary absolute temperature error of 5 K and a noise error of XX K at 86 km altitude. In addition, a second particularly difficult region to retrieve is the tropical tropopause, because measurements below it are likely to be cloud contaminated and because of the very sharp knee in tropopause temperatures.

The TIMED satellite performs six yaw maneuvers per year, changing from a south-looking (83°S–52°N) to a north-looking (52°S–83°N) geometry and vice versa. The relative times of the yaw maneuvers during the year are the same for different years, so that, for instance, SABER always looks to the south in August.

The SABER temperatures are analyzed employing the algorithms described by Preusse et al. [2002]. The global background atmosphere is estimated by a zonal wavenumber 0–6 Kalman filter and subtracted from the individual profiles. This horizontal scale separation approach preserves the vertical spectral information on GWs in the data. Horizontal wavelengths range between the visibility limit of 100-200 km [Preusse et al., 2002] and zonal wavenumber 7. The upper wavelength limit, however, is probably not a serious constraint, since horizontal wavelength estimates from CRISTA [Preusse et al., 2006] indicate that the upper end of the horizontal wavelength distributions follows a ratio of $\omega/f \simeq 1.4$, i.e. is limited by physical processes rather than by the analysis method.

After separation from the background atmosphere, the residual temperature profiles are analyzed by a combination of the maximum entropy method (MEM) and a harmonic analysis (HA), thus providing the amplitudes, vertical wavelengths and phases of the two strongest wave components for each altitude of a measured profile [Preusse et al., 2002]. The width of the sliding vertical window of the harmonic analysis is 10 km.

In this paper, we focus on seasonal variations which are persistent for different years. We therefore bin the data according to calendar months for the almost five-year time series from February 2002 to December 2006, so that, for instance, July values contain data from July 2002, 2003, 2004, 2005 and 2006.

3. GROGRAT ray tracer

3.1. Model description

The observed GW distributions are compared to global GW ray tracing experiments using the Gravity wave Regional Or Global RAy Tracer (GROGRAT). A full description of the GROGRAT model can be found in Marks and Eckermann [1995] and Eckermann and Marks [1997] and we here give a brief summary only. GROGRAT is based on the non-hydrostatic, rotational GW dispersion relation

$$\hat{\omega}^2 = \frac{N^2(k^2 + l^2) + f^2(m^2 + \frac{1}{4H^2})}{k^2 + l^2 + m^2 + \frac{1}{4H^2}}, \tag{1}$$

where $\hat{\omega}$ is the intrinsic frequency, N is the buoyancy frequency, k, l and m are the wavenumbers in x, y and z direction and H is the scale height. The ray tracing equations take into account refraction of the wave vector due to vertical as well as horizontal wind gradients and horizontal gradients of the Coriolis force. Amplitudes are calculated according to wave action conservation. In addition, dissipative processes such as radiative and turbulent damping, which affect also waves with amplitudes well below any saturation criterion, are parameterized.

3.2. Setup of the model experiment

The reliability of a ray tracing experiment largely depends on the choice of the background atmosphere. In the present study, we use ECMWF reanalyses for 0–50 km altitude and winds and temperatures from the TIME-GCM [Roble and Ridley, 1994] for 40–100 km altitude with a smooth transition for the overlapping altitudes [Preusse et al., 2008]. ECMWF reanalysis data are used in numerous transport studies and capture the synoptic scale features of the troposphere and stratosphere well [Borsche et al., 2007; Ern et al., 2007]. For altitudes above the stratopause, data from a TIME-GCM experiment conducted especially for the TIMED mission are used. In order to reproduce the actual atmospheric state, the TIME-GCM is nudged at 30 km altitudes to NCEP reanalyses and radiation-forced migrating tidal components at the lower boundary are provided from the GSWM tidal model [Hagan et al., 1995]. The GCM was run continuously from January 2002 to December 2004 and has been used, for example to analyze tides [Oberheide et al., 2006]. Combining ECMWF and TIME-GCM data, we can therefore generate a realistic background atmosphere matching the actual conditions at the time of the SABER observations.

For the ray-tracing model runs, the data are interpolated to a regular grid with a resolution of 2.5° latitude and 3.75° longitude on 41 pressure levels corresponding to an altitude spacing of 2.5 km. GROGRAT was run in a pseudo-local mode and three wrap arounds in the longitudinal direction were used to prevent rays from leaving the longitude boundaries. Latitudes range from 85 S to 85 N (GROGRAT cannot propagate rays across the pole).

The general outline of the initial launch conditions for the waves follows the one used for the previous GROGRAT–SABER comparison study [Preusse et al., 2006]. A wave is defined by its launch location in terms of latitude, longitude and altitude, propagation direction, horizontal wavelength, phase speed and amplitude. In order to perform a systematic analysis we launched waves homogeneously and isotropically on a regular grid of 20° longitude × 5° latitude in eight directions at every 45° starting from due east. Such a "single spectral component experiment" (SCE) is defined by the horizontal wavelength λ_h, phase speed c_h, wind amplitude $\hat{u}_l$ at launch level and launch altitude. (While SABER measures temperature amplitudes, launch amplitudes for GROGRAT are specified in terms of wind amplitude.) Combining several SCEs, we can emulate a full launch spectrum.

An example of an SCE launch grid is given in Figure 1. The launch locations are indicated by black asterisks. At each launch location rays are launched into eight directions. In addition, the ray traces starting from the zero meridian are shown. The color indicates altitude. Waves propagating versus the wind steepen up and quickly reach the mesosphere, whereas waves propagating with the wind "drift" downstream by many degrees of longitude.

Guided by previous global GW modeling studies as well as online studies of GWs in a GCM [Alexander, 1998; Manzini and McFarlane, 1998; Ern et al., 2004, 2006] we chose a launch altitude of 5 km for all SCEs. Due to computational costs, we have to restrict the number of SCEs. We therefore launch only horizontal wavelengths which match the observational filter of SABER and in particular do not launch short horizontal wavelength waves. As discussed in some depth by Preusse et al. [2006], we know from previous studies that a combination of mesoscale and long horizontal wavelength waves is required. We mimic this by using only two mesoscale horizontal wavelengths covering the full range of phase speeds and only three phase speeds with longer horizontal wavelengths. In particular, the full range of horizontal wavelengths is only covered at $c_h = 30\ \mathrm{ms}^{-1}$ horizontal phase speed. Despite this need for efficiency, we have to launch some SCEs which are discerned only by their amplitudes. Since GWs interact nonlinearly with the background atmosphere, we cannot scale the results after completing the runs. In particular, the launch amplitude determines the saturation altitude. We will discuss this in detail in the following section. The selected components are given in Table 1. Using intermittency factors, we can adapt the contribution of single SCEs to the total GW variance or momentum flux in order to match the observed distribution.

4. Selection of a launch distribution

4.1. Characteristics of single SCEs

The process of selecting single SCEs and choosing suitable intermittency factors follows a trial and error iteration, but is quite straightforward, since the latitude-height cross sections of zonal mean squared amplitudes clearly differ for different components. We will discuss this for zonal mean GW squared amplitudes taken in July. July distributions have a large summer-winter asymmetry. Since the southern polar vortex is stable (except in 2002), the single-day GROGRAT experiment for 15 July is sufficiently representative to choose the wave components. Time series of the typical annual cycle discussed in section 5 then provide an independent test of the chosen launch distribution.

Figure 2 compares zonal mean GW squared amplitudes for vertical wavelengths between 5 and 50 km measured by SABER (panel b) to zonal mean winds (panel a) and to the zonal means from single SCEs (panels c-i). The zonal mean zonal winds are ECMWF-TIME-GCM composites for 15 July 2003, i.e. the zonal mean of the wind field used for the GROGRAT simulations. Details of the SCE launch parameters for the results shown in panels c-i are given in Table 1 together with further SCEs discussed below. For historical reasons, launch amplitudes are specified in GROGRAT as wind amplitudes in ms^{-1}. For all results shown we use squared temperature amplitudes in K^2.

Since not only the amplitude but also the number of rays is important, a background was introduced (cf. detailed discussion in section 4.2 of Preusse et al. [2006]). For the SCEs shown in Figure 2 the background amplitude was chosen to be 0.05 K and both SCE and background are weighted by an intermittency factor of 1. (Please note that this differs from the amplitude value and intermittency factor of older composite experiments given in Table 1.) The intermittency factor is used as a weight applied to the single wave events when averaging over a geographical bin (e.g. a latitude bin at a given altitude in the case of zonal means). The GROGRAT distributions shown in Figure 2 contain only data where the vertical wavelength is between 5 and 50 km and the horizontal wavelength is longer than 100 km in order to mimic the instrument visibility filter (cf. Preusse et al. [2002, 2006]).

The salient features of the measured distribution in panel b) are a general increase in GW squared amplitudes from low to high altitudes, and high values associated with strong winds (cf. panel a) in the southern polar vortex and in the northern subtropics. For the latter, also convective forcing is discussed as an important source [Preusse et al., 2001c; Jiang et al., 2004a; Preusse and Ern, 2005]. At low altitudes a tropical maximum is found, which stretches from about 10° S to the northern subtropics. It presumably consists of long horizontal wavelength, low frequency GWs, which can only exist around the equator because their frequencies are below the Coriolis parameter limit at higher latitudes [Alexander et al., 2002; Ern et al., 2004; Preusse et al., 2006]. These structures are discussed in more detail below.

There is one major difference between the new data shown in Figure 2 and that of the previous investigation by Preusse et al. [2006]. The new data exhibit a strong and monotonic increase of GW squared amplitudes above 80 km in contrast to Figure 2 in Preusse et al. [2006], which shows a decrease of amplitude on top of the southern polar vortex. The old investigation is based on the previous version of SABER data (Version 1.04) and discusses waves with vertical wavelengths between 5 and 25 km. Close investigation of Version 1.04 data shows that above 65 km altitude the temperature profiles appear artificially smooth and that short vertical wavelengths are filtered out completely. The new Version 1.06 data studied in the current paper do not exhibit this artifical smoothing. In addition, we here consider a wider vertical wavelength range (5-50 km). Both effects contribute to the difference. Version 1.06 data analyzed for 5-25 km vertical wavelengths (not shown) exhibit a local maximum associated with the southern polar vortex and a slight decrease directly above (at ∼60-70 km). However, above 85 km we find a monotonic strong increase in GW squared amplitudes also for the shorter vertical wavelength GWs.

The effects of wind filtering and the correlation to the wind fields is strongest for the slow waves, for instance SCE 1 shown in Figure 2c. The strong latitudinal gradients observed in this panel are caused by three mechanisms. First, the waves are much slower than typical wind velocities in the stratosphere and the waves are therefore frequently subjected to critical level filtering when the ground-based horizontal phase speed c_h matches the background wind velocity in the direction of the wave vector ($c_h = U$). Second, the vertical wavelength is refracted by the background winds according to

$$\lambda_z = 2\pi \frac{|c_h - U|}{N} \tag{2}$$

where λ_z is the vertical wavelength and N is the buoyancy frequency. (Equation 2 is valid in mid-frequency approximation.) Since N is about 0.02 s^{-1} in the stratosphere, a 5 km lower limit of the vertical wavelength visibility filter corresponds to an intrinsic phase speed $\hat{c} = |c_h - U|$ of 16 ms^{-1}, which is much faster than the ground-based phase speed of these waves. These waves are thus only visible to SABER and appear in Figure 2 if they are refracted favorably by the background winds. This "visibility effect" was introduced by Alexander [1998]. Third, the maximum temperature amplitude $\hat{T}_{max}$ of a wave before breaking is related to the vertical wavelength by

$$\hat{T}_{max} = \frac{N^2 \overline{T}}{2\pi g} \lambda_z, \tag{3}$$

if we assume convective instability to be the limiting process ($\overline{T}$ the background temperature, g Earth's gravity acceleration). Since, in general, waves grow in amplitude with increasing altitude, long vertical wavelength waves can reach higher amplitudes. All three mechanisms are described in more detail by Preusse et al. [2006].

For the faster waves shown in the lower three rows of Figure 2, the lower limit of the visibility filter (5 km) is sufficiently short to retain most of the waves regardless of the background winds, and visibility effects are therefore less important for the distributions shown in panels d–i. For these SCEs, local maxima and horizontal structures are determined by the wave saturation amplitude and by whether the waves have achieved sufficient amplitudes to be saturated or not. The latter is the difference between panels d and e as well as f and g, respectively. The two SCEs shown in the left row are launched with higher amplitudes $\hat{u}_l$ than their counterparts in the right row. They start to saturate at altitudes of ~50 km (panel d) and ~70 km (panel f). Only above the saturation altitude do GW squared amplitudes form local maxima related to high wind velocities, and on top of the mesospheric jets the GW squared amplitudes decrease. In contrast, the waves shown in panel g (right column) never reach the saturation limit and steadily grow with altitude.

The steady increase of GW squared amplitudes observed in the SABER data (panel b) at high altitudes is therefore an indication of the dominance of fast waves at high altitudes (>80 km). The launch amplitudes given in Table 1 demonstrate that if these waves originate in the troposphere or lower stratosphere (TLS) they could hardly be detected close to their source altitude by any measurement technique because of their very low amplitudes. On the other hand, this means that there is a good likelihood of such waves being forced by background fluctuations.

Figure 2i shows long horizontal wavelength waves. Their ground-based frequency $\omega_{gb} = c_h/(2\pi\lambda_h)$ is lower than the Coriolis parameter f at most latitudes. Therefore at low altitudes these waves can only occur around the equator. At higher altitudes they can escape this confinement if they propagate opposite to strong background winds and therefore adopt higher intrinsic frequencies. Long horizontal wavelength waves are therefore likely responsible for the tropical maximum observed in Figure 2b as well as a number of in situ and satellite observations [Alexander et al., 2002; Ern et al., 2004; Preusse et al., 2006].

Fast waves of long horizontal wavelengths shown in Figure 2h are not generally prohibited by the dispersion relation at higher latitudes, but are more likely subject to wave damping and critical level filtering than their mesoscale counterparts (e.g. the SCEs shown in panels f and g). Since they are also able to propagate far away from their sources, such waves can best match the sloped isolines of the SABER observations for mid and high northern latitudes (close to 45° slope between 30°N and 70°N in Figure 2b) .

4.2. Choice of the intermittency factors

The comparison of single SCEs with the measurements in Figure 2 gives us a general guidance for composing a launch “spectrum” from a number of SCEs. Additional constraints can be gained from high vertical resolution observations of a universal spectrum of GWs [Fritts, 1984; Tsuda and Hocke, 2002; Fritts and Alexander, 2003] indicating that GWs with vertical wavelengths shorter than 2-4 km in the stratosphere are saturated. In addition, horizontal wavelength and momentum flux distributions from CRISTA [Ern et al., 2004, 2006], which had twice as dense horizontal sampling as SABER, can give further guidance [Preusse et al., 2006].

We now generate composites from the single SCEs guided by the comparison in subsection 4.1. Following an educated guess, different composites can be generated by choosing different intermittency factors (IMFs). For each altitude and geographical bin defined by its latitude (and in case of maps) longitude boundaries the single wave events are weighted by the IMFs when calculating an average. Some examples of different composites are given in Figure 3. Panel a repeats the SABER zonal mean cross section from Figure 2b, panels b-g show five different experiments with IMFs as listed in Table 1.

Figure 3c uses the same intermittency factors as the previous experiment by Preusse et al. [2006]. However, despite equal IMFs there are differences between the setup used by Preusse et al. [2006] and the setup of the results shown here. First, the old experiment is for August 1997 whereas we here use wind data for July 2003. Second, the old experiment is based on a combination of ECMWF data and CRISTA geostrophic winds whereas the new one is based on ECMWF data and TIME-GCM simulations for the higher altitudes and thus covers a wider latitude range, and finally we use a wider vertical wavelength filter for the new results shown in Figure 3. Figure 8 a-d of Preusse et al. [2006] therefore shows similar (note the different color scales), but not identical results to those in Figure 3c.

The main shortcoming of the composition chosen by Preusse et al. [2006] is the overestimation of GW squared amplitudes at the high summer latitudes. In addition, after the change from Version 1.04 to 1.06 and by taking into account longer vertical wavelengths we observe a monotonic increase of GW squared amplitudes at high altitudes. These two aspects motivated us to modify the old composition of Preusse et al. [2006]. We removed the contribution of fast waves launched with non-saturated, but notable amplitudes (SCEs 7 and 13) and replaced them by fast waves launched with very small amplitudes (SCEs 9 and 15). This composite Exp04 is shown in Figure 3d. The composite is improved in that it does not greatly overestimate the high latitude summer values, but as a side effect the GW squared amplitudes between 30°S and the equator are now underestimated. In addition, this modification does not improve the agreement between measurement and modeling at high altitudes above 80 km.

To match both relatively high values at the equator and the gradual spread of GW variances towards high summer latitudes, i.e. the fact that isolines between 20N and 80N are tilted about 45° in Figures 2b and 3b, motivated us to introduce a component with long horizontal wavelength and fast phase speed (SCE 23, Figure 2h). In addition, there is an identical SCE differing only in the launch amplitude (SCE 22, not shown).

Experiments 14, 32 and 232 (panels e-g) introduce these new SCEs using different sets of intermittency factors (IMFs). Experiment 32 and 232 differ in the horizontal wavelengths of the mesoscale waves, i.e. SCEs 2, 4, ... 18 with 500 km horizontal wavelength each replace SCEs 1, 3, ... 17 with 200 km horizontal wavelength, respectively.

As the experiment numbers indicate, the choice of the "optimal" composite is based on a trial and error procedure varying the intermittency factor and picking a result which is in good agreement with the observations. However, Figure 3 shows that experiments 32 and 232 are almost indiscernible in GW squared amplitudes. Therefore we need additional data to constrain the horizontal wavelength and compare absolute values of momentum flux from the ray tracing experiments to CRISTA momentum flux estimates.

CRISTA took measurements during two one-week periods in October 1994 (CRISTA-1) and August 1997 (CRISTA-2) [Offermann et al., 1999; Riese et al., 1999; Grossmann et al., 2001]. Both missions have been analyzed for absolute values of GW momentum flux [Ern et al., 2006]. Momentum flux can be inferred from temperature variations by equation (7) of Ern et al. [2004] if both the horizontal wavelength and the vertical wavelength of the wave are known :

$$F_{ph} = \frac{1}{2}\rho\frac{k_h}{m}\left(\frac{g}{N}\right)^2\left(\frac{\hat{T}}{T}\right)^2 \qquad (4)$$

where $k_h = 2\pi/\lambda_h$ is the horizontal wavenumber, $m = 2\pi/\lambda_z$ is the vertical wavenumber, $\hat{T}$ is the temperature amplitude, and ρ, N and T are density, buoyancy frequency and temperature of the background atmosphere. The horizontal sampling distance of CRISTA was ∼200 km, which implies a Nyquist wavelength (i.e. shortest resolvable wavelength) of 400 km. Ern et al. [2004] showed that CRISTA data undersample the measured GWs and that some effects of aliasing occur when inferring horizontal wavelength distributions. The horizontal sampling distance of SABER is twice as large as the CRISTA sampling distance and therefore too coarse to retrieve momentum flux estimates for GWs.

Figure 4 compares absolute values of GW momentum flux measured by CRISTA-2 (Aug. 1997, panel a) and CRISTA-1 (Nov. 1994, panel e) with GROGRAT results for composites 32 (b, f), 132 (c, g) and 232 (d, h) calculated for 15 Aug. 2003 (b-d) and 15 Nov. 2003 (f-h). The difference between the three composites is the horizontal wavelength. Composite 32 uses λ_h =200 km for all mesoscale components, composite 132 uses λ_h =200 km for the fast waves and λ_h =500 km for the slow waves, which dominate the lower altitudes, and composite 232 uses λ_h =500 km for all mesoscale components. An observational filter of $\lambda_z = [5, 20]$ km is applied to the GROGRAT results. Note that due to the observational filter GW-MF can increase with increasing altitude. This is observed, for instance, at the summer polar mesopause. Although for every individual wave momentum flux decreases with altitude this is possible because some waves carrying large GW-MF are refracted in vertical wavelengths, shift into the range of the observational filter, and become visible in the zonal means.

From (4) we expect the 500 km horizontal wavelength waves to carry a factor of 2/5 less momentum than the 200 km waves, which corresponds to an offset of ∼4 dB in Figure 4. In agreement with Preusse et al. [2006], we find that momentum flux distributions based on a typical wavelength of 500 km for the mesoscale waves match the observations well, whereas assuming a typical wavelength of 200 km overestimates the GW momentum flux. Composite 132, which combines 500 km horizontal wavelength for the slower and 200 km horizontal wavelength for the faster mesoscale SCEs (cf. Table 1), is very similar to composite 232 in the stratosphere. This means that the horizontal wavelengths of the very fast waves with small launch amplitudes cannot be sufficiently constrained by the CRISTA stratospheric observations.

Overall, composite experiment 232 matches the observations best. GW squared amplitudes show low values in the summer hemisphere and tilted isolines at a similar angle as the observations, reasonably high values at the equator and a monotonic increase in the upper mesosphere. The momentum flux values are compatible with the CRISTA measurements. We therefore choose composite experiment 232 for further discussion.

5. The annual cycle in SABER and GROGRAT GW results

5.1. Global maps in the lower stratosphere

SABER:

Figure 5 shows global maps at 28 km altitude of GW squared temperature amplitudes of the strongest wave component for vertical wavelengths between 5 km and 50 km. The data are binned to a 1° latitude × 2° longitude grid by a triangular weight of 800 km width, i.e. a SABER point is weighted 1 if it coincides with a grid point, weighted zero if the distance between SABER point and grid point is larger than 800 km, and weighted with a linearly interpolated value between 0 and 1 for distances in between.

The maps for the two solstices (January and July) are essentially flipped with respect to the equator and are both very different from the two maps at equinox (April and October). At the solstices a very pronounced winter vortex maximum is the dominant feature and a secondary maximum can be found in the tropics and subtropics of the summer hemisphere. The GW variances at high summer latitudes are very low. These are all features well known from GW temperature variances extracted from a number of different satellite instruments [Wu and Waters, 1997; Ern et al., 2004, 2006; de la Torre et al., 2006]. The summer low latitude maximum is commonly attributed to convectively generated GWs in the monsoon regions and above high sea surface temperature regions and correlates well with cloud proxies [McLandress et al., 2000; Preusse et al., 2001c; Jiang et al., 2004a; Preusse and Ern, 2005]. The comparison of July and August values shows that the most active region in Asia shifts eastward from the Indian monsoon towards the Kuro-Shio ocean stream. This more eastward position of wave activity is very similar to the CRISTA observations [Preusse et al., 2001c; Ern et al., 2004] and is connected with a further northward shift into the subtropics. It should also be noted that a high GW momentum flux in the summer subtropics was explained, at least to some extent, by wind filtering [Ern et al., 2004].

There are two noticeable differences between the two respective hemispheres. First, the wave activity in the winter vortex is stronger and much more uniform (i.e. it lacks significant longitude dependence) for the southern hemisphere (SH) due to a more stable winter polar vortex. Second, the subtropical band of high wave activity extends further northward in July than southward in January, which might be due to a more pronounced monsoon season in the northern hemisphere (NH).

At the equinoxes, tropical GW variances are symmetric about the equator. In general, GW variance is much less pronounced than at the solstices. At higher latitudes wave activity is often found over regions where orography could contribute to the forcing as for instance above the southern tip of South America and the Eurasian continent. This agrees with previous studies by Eckermann and Preusse [1999] and Jiang et al. [2002, 2004b] modeling GW activity found in CRISTA and MLS data with the NRL mountain wave forecast model (NRL-MWFM).

GROGRAT:

Figure 6 shows global maps at 28 km altitude of GROGRAT GW squared temperature amplitudes from composite Exp232 for vertical wavelengths from 5 km to 50 km. The ray traces are calculated for 12 GMT on days 3, 6, 9, ... and 27 of the respective month in 2003 and 2004. This should provide a sufficiently large database to obtain a realistic average of strong planetary waves in the northern winter, highly variable tropospheric weather conditions and different QBO phases.

However, the GROGRAT modeling assumes a homogeneous and isotropic GW source and therefore does not include strong localized GW sources such as orography or deep convection.

The modeled fields reproduce the observations in many respects, such as the asymmetry between northern and southern hemisphere with respect to the polar vortex and the absence/presence of strong planetary waves modulating the GW activity in the polar vortex as well as the shift of GW activity into the summer hemisphere in the tropics and the symmetry with respect to the equator for the equinoxes. In addition, the seasonal cycle of GW squared amplitudes in the southern polar vortex is quite well reproduced: an absence of wave activity in January; the build-up of the vortex wave activity in April; strong, almost zonally symmetric wave activity in July; and a decaying vortex disturbed by planetary waves in October. In January measurement and model agree in the position of the high latitude maxima of GW squared amplitudes above eastern Europe and central Asia (30° E – 90° E) and at the east coast of North America. The position of the maxima reflects the preferential phase of the planetary waves and hence the position of the vortex edge in the northern hemisphere winter.

However, for northern hemisphere winter the magnitude of GW activity in the model is much smaller than in the observations and the model exhibits a much stronger asymmetry between southern and northern hemisphere winter polar vortex values than the measurements, which show essentially equal peak values for the southern hemisphere in July and the northern hemisphere in January. A possible explanation is that weaker winds in the northern hemisphere are compensated by orographic forcing of the numerous mountain ranges in the northern hemisphere, for instance the south tip of Greenland, the Norwegian mountain ridge the Alps and the Urals, which are all prominent sources of stratospheric GWs [Eckermann and Preusse, 1999; Dörnbrack and Leutbecher, 2001; Jiang et al., 2004b]. Interestingly, even in this five year climatology we do not find enhanced amplitudes above the Rocky Mountains, which is in agreement with previous studies [Eckermann and Preusse, 1999; Jiang et al., 2004b]. In contrast to the northern hemisphere, orography is responsible only for a small fraction of the waves observed in the SH winter; that is orographically forced waves above the south tip of South America and the Antarctic Peninsula [Eckermann and Preusse, 1999; Jiang et al., 2002; Ern et al., 2006].

Furthermore, the high GW squared amplitudes over the Gulf of Mexico and the Asian monsoon regions are not reproduced, indicating that these are features generated primarily by convective sources rather than by the modulation of GWs by the background winds. The same likely applies for the observed enhanced GW activity in the tropics/subtropics in January, which is not reproduced by the model (there is a southward shift, but no real enhancement in Figure 6a).

5.2. July maps in stratosphere and mesosphere

SABER:

Figure 7 shows GW squared amplitudes in July, same as Figure 5c, but for altitudes from 40 km to 70 km. At 40 km altitude we find the same subtropical maxima as for 28 km altitude. These structures are somewhat less pronounced with respect to the background GW variances at 50 km, but still noticeable. At 60 km and 70 km altitude, however, the structure becomes more band-like (i.e. lacks longitudinal variation) and is further shifted to the north. There are two likely explanations for this behavior. First, as altitude increases waves propagate further away from their sources. The source patterns therefore smear out. Second, smaller waves with less pronounced sources or from a GW background can grow and attain larger amplitudes. The influence of the wind fields becaomes more important than the influence of the sources at higher altitudes.

GROGRAT:

At higher altitudes GROGRAT still largely resembles the observations as can be seen from Figure 8. The absolute values at the respective altitudes and the relative strength of the southern polar vortex and the northern subtropical maximum agree well. Of course, GROGRAT can neither reproduce the convectively forced GWs above Florida and the Asian Monsoon regions nor the loss of these features with altitude. Further, a general underestimate of GW squared amplitudes in the southern subtropics points to the dilemma of either overestimating the high summer latitudes or underestimating the tropical and subtropical values of the winter hemisphere. This problem has already been discussed in section 4.2 and has been remedied but not solved by the new launch distribution.

5.3. Time series of zonal mean squared amplitudes

Figure 9 compares time series of zonal mean squared GW amplitudes measured by SABER (left column) with the results from GROGRAT composite experiment 232 (right column). Again, the GROGRAT result average over every third day of the respective months in 2003 and 2004. Altitudes between 30 km and 90 km are shown and in general good agreement between observed and modeled structures is found.

At 30 km altitude, SABER observes high GW squared amplitudes in the winter polar vortices. They contrast with very low GW activity in the summer mid and high latitudes. In the tropics and subtropics, the phase of the annual cycle is reversed and maxima for the SABER measurements are found after the summer solstice, i.e. values are maximum in July and August in the northern hemisphere and maximum in January and February in the southern hemisphere. The high latitude maxima shift to early winter at 50 km altitude whereas the subtropical maximum remains fixed in time. This is in agreement with Fig. 2f of Krebsbach and Preusse [2007], which shows the altitude-latitude variations of the maximum of the annual cycle deduced from SABER GW analyses. Krebsbach and Preusse [2007] find a downward progression of phase in the polar vortices but an almost constant phase throughout the entire stratosphere for the subtropics.

The GROGRAT modeling reproduces the enhanced wave amplitudes in the winter polar vortices well, and also the shift towards earlier months at increasing altitude. The hemispheric asymmetry between the very large GW squared amplitudes in the southern hemisphere winter polar vortex and the somewhat weaker values in the northern hemisphere winter polar vortex is even more pronounced in the GROGRAT model results. As discussed in section 5.1, a potential explanation is that the GROGRAT simulation does not take into account the enhanced forcing of GWs by orography.

The subtropical maximum is less pronounced in the GROGRAT modeling than in the observations. The difference further supports the assumption that the observed maxima are caused to a large extent by convection during the monsoon and above regions of high sea surface temperature (SST), as has been found from correlations of GWs to cloud proxies and SST [McLandress et al., 2000; Preusse et al., 2001c; Jiang et al., 2004a; Ern et al., 2004; Preusse and Ern, 2005].

At 70 km altitude (Figure 9e and f) the summertime subtropical maxima extend further poleward and around 30° latitude we find both the winter polar jet and the summer time maxima. This results in an apparent semi-annual oscillation signal between 30° and 50° in both hemispheres. We will discuss this feature in more detail in section 6.

At 95 km altitude the GROGRAT model results underestimate the SABER values by about 4 dB. The most interesting feature in both measurements and model results is a high latitude summer maximum. Which waves cause this phase reversal of the annual cycle between 70 km and 95 km altitude? Figure 10 compares time series of slow (SCEs 4 and 8, cf. Table 1) and fast mesoscale waves (SCEs 16 and 18) as well as fast long horizontal wavelength waves (SCEs 22 and 23) for 80 and 95 km altitude. At 80 km altitude, all SCEs exhibit a wintertime maximum at mid and high latitudes. The wind reversal between 80 km and 95 km altitude removes most of the very slow waves (SCE 4; $c = 10$ ms^{-1}) and reduces the GW squared amplitudes of SCE 8 with $c = 30$ ms^{-1} phase speed. However, the remaining GW activity of these slower waves still has a wintertime maximum also at 95 km altitude. With increasing phase speed (SCEs 16 and 18; $c = 51$ ms^{-1} and $c = 90$ ms^{-1}) a pronounced summertime maximum arises for the mesoscale waves. This is not the case, however, for the long horizontal wavelength waves (SCEs 22 and 23; $\lambda_x = 200$ km) though they are comparable in amplitude and phase speed ($c = 60/61$ ms^{-1}) with the fast mesoscale waves.

Only the fast mesoscale waves can cause the phase reversal and the fact that we observe the phase reversal in the measurements as well as in the composite experiment shows that these waves dominate the upper altitudes in reality as well as in the model.

The reproduction of the reversal of the annual cycle around the mesopause by composite 232 therefore supports that the intermittency factors are chosen reasonably. Also, since we did not use the annual cycle for tuning the intermittency factors, the physical explanation increases confidence that the interpretation of the residual temperature fluctuations in terms of GWs still makes sense around the mesopause and in the lower thermosphere.

5.4. Annual cycle of GW momentum flux

Figure 11 shows time series of zonally averaged absolute values of GW momentum flux from GROGRAT composite experiment 232 (cf. Table 1) filtered to retain vertical wavelengths $\lambda_z = [5, 25]$ km. In August we find a fully developed southern polar vortex and northern subtropical maximum. Both decay in boreal fall and only weak remnants are found in November. This explains the differences between the August and November distributions shown in Figure 4.

In addition to CRISTA data, there is one further data set that provides global estimates of GW momentum flux. Alexander et al. [2008] analyze HIRDLS data for May 2006. They find much lower momentum flux values of about -27 dB (i.e. -2.7 log_{10} Pa) in the polar vortex and -35 dB in the subtropical maximum at 25 km altitude and -35 dB in the polar vortex and -44 dB in the subtropical maximum at 45 km altitude. HIRDLS data are therefore much lower than the CRISTA values in Figure 4. In addition, HIRDLS data display a stronger contrast between the southern polar vortex and the subtropical maximum. The latter can be explained from Figure 11. In May the southern polar vortex is already pronounced whereas the subtropical maximum is just starting to develop.

Potential reasons for the much lower magnitude of the HIRDLS GW momentum flux values include a different vertical wavelength observational filter, the visibility and aliasing corrections made for CRISTA [Ern et al., 2004] and the analysis method itself. To resolve this puzzle merits further investigation but goes beyond the frame of this study.

6. Propagation direction and distance, momentum flux and mean flow acceleration

As pointed out in section 4, the choice of wave components and intermittency factors is based only on boreal summer results. The annual cycle of GW squared amplitudes from SABER therefore provides an independent test basis. The good agreement found between observations and model results supports the choice of SCEs and intermittency factors deduced from boreal summer observations. Though there are still deviations between the observations and the model results, probably mainly due to unresolved GW sources, we have now gained sufficient confidence in the model results to infer quantities which cannot be inferred from the measurements themselves.

6.1. Time series of zonal propagation direction

An open question which can be answered by such inferred quantities is the nature of the strong mid-latitude semiannual variation found in the mesosphere. Krebsbach and Preusse [2007] spectrally analyzed a four- year data series of root mean square (RMS) zonal averages. Around 70 km they found about 2.0-2.5 K semiannual amplitude for 40° latitude in both hemispheres, but only 0.5-1.0 K semiannual amplitude in the tropics where we expect to find modulation of GWs by the well-known mesospheric semiannual oscillation (SAO) in the tropical zonal winds [Hirota, 1978; Burrage et al., 1996]. Krebsbach and Preusse [2007] speculated that the variations at 40° latitude are not SAO signals but rather an annual cycle, if GW momentum fluxes were considered. This is supported by Figure 9e. Between 25° and 50° latitude we find an overlap of the GW activity related to the polar vortex spreading equatorward and the subtropical maximum spreading poleward. From the zonal winds, we expect opposite preferential propagation directions for the two maxima. We test this hypothesis by calculating the average zonal momentum flux shown in Figure 12.

The color scale in Figure 12 indicates the absolute value of the zonal momentum flux, overplotted solid lines indicate positive values, i.e. preferentially eastward propagating waves, overplotted dashed lines indicate negative values, i.e. preferentially westward propagating waves. As expected, waves propagate preferentially eastward against the subtropical easterly jet in the summer of the respective hemisphere and preferentially westward against the polar vortex jet in winter. At the equinoxes, the average zonal momentum flux vanishes. Figures 9e and f still show significant GW activity at these times, i.e. the vanishing zonal momentum flux is caused by the compensation of waves propagating in different directions rather than by an absence of waves.

6.2. Acceleration

The GW-induced forcing is given by Equ. 42 of Fritts and Alexander [2003]:

$$\left(\bar{X}, \bar{Y}\right) = -\frac{\epsilon}{\bar{\rho}} \frac{\partial}{\partial z} \left(F_{px}, F_{py}\right), \tag{5}$$

where (F_{px}, F_{py}) is the horizontal vector of the vertical flux of GW momentum, $\bar{\rho}$ is the density of the background atmosphere, and $\left(\bar{X}, \bar{Y}\right)$ an acceleration term for the background flow. Conventionally, the equation contains an intermittency factor ϵ reflecting the fact that GWs might not always be present in the atmosphere. Since the derivative is commutative with the averaging of the single wave components we calculate the acceleration for the GROGRAT composites by

$$\left(\bar{X}, \bar{Y}\right) = -\frac{1}{\bar{\rho}} \frac{1}{N} \sum_i \epsilon_i \frac{\partial}{\partial z} \left(F_{px,i}, F_{py,i}\right) \tag{6}$$

where N is the number of the single GWs i in the considered bin (e.g. latitude bin at fixed altitude for zonal means) and ϵ_i is an intermittency factor associated with this wave according to Table 1. Note that in this way the final obliteration of a wave near a critical level does not contribute to the acceleration, because we do not take into account the disappearance of waves between different altitude levels. However, since the vertical wavelength, and therefore the saturation amplitude, becomes very small before a GW encounters a critical level, the error due to this neglect is small if the vertical binning is sufficiently fine (we used 1 km vertical binning).

In GROGRAT the waves can be horizontally refracted by horizontal gradients of the background wind. Therefore there are two different mechanisms for transferring momentum to the mean flow. First, the waves can dissipate by wave breaking or turbulent and radiative dissipation. In this case, the acceleration is given by the vertical gradient of the absolute value of momentum flux $|F_p|$ in the direction of the horizontal wave vector (k, l)

$$\left(\bar{X}, \bar{Y}\right)_{diss} = -\frac{1}{\bar{\rho}} \frac{1}{N} \sum_i \epsilon_i \frac{(k, l)}{k^2 + l^2} \frac{\partial}{\partial z} |F_p| \tag{7}$$

Second, waves can change their horizontal propagation direction. For instance, a wave propagating northeastward might be aligned more zonally with increasing altitude. In this case, the wave carries less meridional and more zonal momentum. The acceleration is then expressed by the change of the wave direction. If ϕ is the direction of the wave vector defined counterclockwise from due east (ϕ =0), the acceleration by wave turning is

$$\left(\bar{X}, \bar{Y}\right)_{turn} = -\frac{1}{\bar{\rho}} \frac{1}{N} \sum_i \epsilon_i |F_p| \frac{\partial}{\partial z} \left(\cos(\phi), \sin(\phi)\right) \tag{8}$$

In addition to these two mechanisms there are further effects in GW theory which influence the momentum and amplitudes of GWs. When GWs are refracted by horizontal gradients also the wavelength of the wave and the area covered by the wave-packet change. These two effects would have to be considered simultaneously, but the area spread effect cannot be incorporated easily into a model based on a very limited number of single rays. We therefore decided to neglect these effects and first investigate the GW forcing mechanisms described above.

Figure 13 shows zonal mean accelerations for composite 232 for 15 July 2003. It should be noted that we do not apply visibility filters for acceleration calculations. The left column shows the acceleration in the zonal direction and the right column the acceleration in the meridional direction. All waves which do not propagate purely zonally or purely meridionally contribute to both forcing terms. The uppermost row shows the total acceleration from Equ. (6). Values of $\bar{X}$ (Figure 13a) can reach up to 250 $\mathrm{ms^{-1}day^{-1}}$ at the summer mesopause (we limited the color scale in order to visualize the accelerations in the upper stratosphere and lower mesosphere). This is of the same order but at the high end of the acceleration values generally reported from GCM and GW parameterization studies (e.g. McLandress [1998]; Charron et al. [2002]; McLandress and Scinocca [2005]).

Does the fact that the observed waves are already sufficient to explain all the wave forcing needed by the GCMs mean that meso- and largescale waves exclusively drive the MLT? When considering these values we should keep in mind that the GW accelerations shown are a pure forward result from the tuning of the launch values and intermittency factors by the measured GW-amplitudes in particular in July and some further constraints on GW momentum flux measurements in the stratosphere. The observed reasonable value and structure for the acceleration terms is therefore already an achievement.

As pointed out above, there is in particular a complete lack of constraints on the horizontal wavelength distribution in the mesosphere and there still remains great freedom for tuning. In addition, in our study some serious assumptions are made. For instance, we do not consider any processes that could transport momentum away from the dissipation regions such as secondary wave generation [Vadas and Fritts, 2002] or non-linear wave interaction, for example, by triads [Bittner et al., 1997; Wüst and Bittner, 2006]. We also assume that all waves propagate upward whereas in the real atmosphere at least some waves will propagate downward. However, the amount of downward-propagating GWs is not well known in the middle atmosphere, because there are no experimental constraints for the fraction of downward-propagating waves for the upper stratosphere and lower mesosphere. It should be noted in this context that wave reflection occurs when the intrinsic frequency $\hat{\omega}$ approaches the buoyancy frequency and does not occur for the mesoscale and long horizontal wavelength (>100 km) GWs observed by IR limb sounders considered in this study (cf. Kim et al. [2003]; Fritts and Alexander [2003]; Preusse et al. [2008]). Downward propagating waves in this wavelength regime therefore can only originate from high altitude sources.

For the above-mentioned reasons, our acceleration values are likely overestimated. Short horizontal wavelength GWs observed by airglow imagers are also known to carry significant momentum [Tang et al., 2005]. Short and mesoscale waves therefore both contribute to driving the wind systems and circulation in the MLT. The uncertainties of this study are too large to really address the relative role of the different wavelength regimes quantitatively. However, the results shown suggest that meso- and large-scale gravity waves are important.

Figure 13b shows the meridional acceleration $\bar{Y}$. The meridional accelerations are about a factor three smaller (again the color scale is limited in order to highlight structures in the upper stratosphere and mesosphere). The fact that the meridional accelerations are smaller than the zonal accelerations is caused by the preferentially zonal direction of the mean flow. It is also observed in GCM studies.

The middle row shows the contribution of wave turning due to GW refraction in horizontal wind gradients calculated from Equ. (8). The lowermost row gives the relative contribution of this term to the total forcing. Values are only shown if the total acceleration is larger than 5 $ms^{-1}day^{-1}$. The zonal acceleration by wave turning (Figure 13c) remains smaller than 5 $ms^{-1}day^{-1}$ and contributes less than 5 % (Figure 13e). Thus from the zonal GW induced forcing alone this effect could be neglected. However, the absolute values as well as the relative contributions in the meridional direction are larger (Figure 13d, f). Relative contributions of wave turning to the meridional forcing can exceed 50 %. By comparing panels b) and d) it can be seen that wave turning acts at different locations and sometimes counteracts acceleration by dissipation. Though the uncertainties of the results shown are still large, Figure 13 indicates that this effect merits further consideration.

6.3. Zonal propagation

Gravity wave parameterization schemes operated in GCMs generally assume that GWs propagate upward in the vertical column of a GCM grid point. (There is one exception: the ray-tracing parameterization of convectively generated GWs by Song and Chun [2008].) However, GWs propagate along their phase fronts and since the GWs we consider have much longer horizontal than vertical wavelengths we can expect that they cover considerable distances in the horizontal when propagating from the troposphere into the mesosphere. An impression of this is given in Figure 1. Some of the waves shown travel once around the globe and some cross 40° or more in latitude. However, is this representative and are the waves that propagate over large distances the same waves which convey large momentum flux?

Zonal means of the latitude difference between the launch location and the actual position of the GW rays in the atmosphere are shown in Figure 14. Negative values indicate that the waves preferentially originate from sources northward of the observation latitude (i.e. southward-propagating waves), positive values indicate that the rays stem preferentially from the south (i.e. northward propagation). Low values can indicate a zonal alignment of the wave vectors and fast upward propagation or a balance of northward- and southward-propagating waves.

At very high latitudes we are close to the model grid boundaries and GWs propagating toward the lateral boundaries, i.e. poleward-propagating GWs, cannot be compensated by waves propagating in the opposite direction, since these waves would need to originate from outside the grid. The high values observed at very high latitudes ($>60^\circ$) are therefore artificial and in the following we discuss low and mid lattitudes ($<60^\circ$) only.

As expected, the average latitude shift increases with increasing altitude in Figure 1. A large part is contributed by long horizontal wavelength waves which can exist at low altitudes only in the tropics and spread poleward with increasing altitude (cf. Figure 2i). Consequently, when weighting the latitudinal shift by the momentum flux of the waves (Figure 14b), the values are strongly reduced. However, when weighting the latitudinal shift by the accelerations, in particular in the stratosphere and lower mesosphere the slower waves are emphasized and the latitudinal shift is enhanced. Even though accelerations at these altitudes are small they should contribute significantly to the branch of the Brewer-Dobson circulation in the summer hemisphere [Alexander and Rosenlof, 2003]. In a changing climate, the wind fields in the troposphere and stratosphere will change. A propagation path of the waves that differens from the one assumed in tuning the parameterization scheme for the needs of the GCM then might induce an incorrect response to climate change.

7. Conclusions

In this paper, we derived a climatology of GW squared amplitudes from the Sounding of the Atmosphere using Broadband Emission Radiometry (SABER) temperatures mapping a five-year time series on the calendar months. Many salient features are compatible with previous observations from different satellites showing these features to be persistent in different years.

The measurements are compared to global ray tracing studies employing the Gravity wave Regional Or Global RAy Tracer (GROGRAT). Based on SABER zonal mean GW squared amplitudes for July and CRISTA momentum flux values, a homogeneous and isotropic launch distribution is inferred. The launch distribution contains different phase speed mesoscale waves, some of very high phase speed and extremely low amplitudes, as well as long horizontal waves of several thousand km horizontal wavelength. Waves are launched in eight directions at 5 km altitude.

The tuning of the launch distribution is based on zonal means and July values only. Comparisons between measurements and model results for global maps revealing longitudinal structures and time series of the annual cycle therefore provide independent tests. The good agreement found raises confidence in the chosen launch parameters. In particular, the time series show a reversal of the phase of the annual cycle between 80 km and 95 km altitude. This phase reversal is caused by mesoscale waves with high phase speeds greater than 50 ms^{-1}.

Based on this realistic observation-tuned model run, we can calculate quantities which cannot be addressed by the SABER measurements and are speculated to be major sources of uncertainty in current-generation GW parameterization schemes. Two examples shown in this paper are the average cross-latitude propagation of GWs and the relative acceleration contributions provided by saturation and dissipation, on the one hand, and the horizontal refraction of GWs by horizontal gradients of the mean flow, on the other hand.

The average cross-latitude propagation reaches peak values of about 15°. Long horizontal wavelength waves carrying little momentum largely contribute to this value and as a consequence momentum flux weighted mean values are much lower. However, acceleration weighted values even reach up to 25° average cross-latitude propagation in the stratosphere and lower mesosphere. Though these accelerations are small in absolute numbers they likely provide an important contribution to the summer Brewer-Dobson circulation [Alexander and Rosenlof, 2003]. In a changing climate, the wind fields in the troposphere and stratosphere will change. A propagation path of the waves that differs from the one assumed in tuning the parameterization scheme for the needs of the GCM then might induce an incorrect response to climate change.

Both zonal and meridional GW induced mean flow forcing are of the same order but at the upper end of the range known from GCM and GW parameterization scheme studies. Error ranges are high, however, since we have very few constraints on the horizontal wavelength distributions in particular on the fast waves carrying large momentum into the MLT. In addition, the current approach neglects processes which could carry away momentum flux from regions of wave instability, such as secondary wave generation.

Despite these caveats we have a sufficiently realistic simulation to test whether the horizontal refraction of GWs by horizontal gradients of the background winds is an important effect on a global scale compared to momentum deposition by wave dissipation. Mean flow forcing by horizontal refraction was introduced by Bühler and McIntyre [2003] as a new mechanism acting at different locations and in a different way than wave dissipation and therefore is called "remote recoil". However, Bühler and McIntyre [2003] provided only a theoretical explanation of the effect and did not estimate the relative magnitude compared to wave dissipation in the real atmosphere. We here find that the effect is smaller than 5 % for zonal acceleration, but up to 50 % in meridional acceleration and therefore merits further consideration.

The GROGRAT model results match the observed distributions well. However, they cannot answer the question of which source should be omnipresent at 5 km altitude. In addition, global maps already indicate missing sources such as orography and deep convection. In future, we therefore will need to replace a tuned parameterized source distribution by real understanding.

In order to reach this aim a better characterization of the observed waves is required [Alexander and Barnet, 2006]. Major sources of uncertainty also for the current study are horizontal wavelength distributions and direction characteristics. Some first attempts to investigate horizontal wave structures were made by Eckermann and Preusse [1999] and Preusse et al. [2002], and recently some interesting studies have been based on nadir viewing instruments [Wu and Zhang, 2004; Alexander and Barnet, 2006; Eckermann et al., 2006]. However, nadir viewing satellites can capture only a small part of the vertical wavelength distribution at the low altitudes where they are sensitive. What is urgently needed is an instrument with the good vertical resolution of a limb sounder and the good horizontal mapping of a nadir viewing instrument. Employing infrared limb-imaging such an instrument can be build based on recent advances in detector technology [Riese et al., 2005; **?**].

8. Acknowledgments

Please send in your acknowledgments!

References

Achatz U. (2007), The primary nonlinear dynamics of modal and nonmodal perturbations of monochromatic inertia-gravity waves, J. Atmos. Sci., 64, 74-95.

Alexander, M. J. (1998), Interpretations of observed climatological patterns in stratospheric gravity wave variance. J. Geophys. Res. 103, 8627-8640.

Alexander, M. J., and T. J. Dunkerton (1999), A Spectral Parameterization of Mean-Flow Forcing due to Breaking Gravity Waves, *J. Atmos. Sci., 56*, 4167-4182.

Alexander, M. J., Tsuda, T., Vincent R.A. (2002), On the latitudinal variations observed in gravity waves with short vertical wavelengths. J. Atmos. Sci. 59, 1394-1404.

Alexander, M. J., and K. H. Rosenlof (2003), Gravity-wave forcing in the stratosphere: Observational constraints from the Upper Atmosphere Research Satellite and implications for parameterization in global models, *J. Geophys. Res., 108*, 4597, doi:10.1029/2003JD003373.

Alexander, M.J., and C. Barnet (2007),Using satellite observations to constrain parameterizations of gravity wave effects for global models, J. Atmos. Sci., 64, 1652-1665.

Alexander, M. J., J. Gille, C. Cavanaugh, M. Coffey, C. Craig, V. Dean, T. Eden, G. Francis, C. Halvorson, J. Hannigan, R. Khosravi, D. Kinneson, H. Lee, S. Massie, B. Nardi, A. Lambert, (2008), Global Estimates of Gravity Wave Momentum Flux from High Resolution Dynamics Limb Sounder (HIRDLS) Observations, *J. Geophys. Res.,* in print.

Allen, S. J., and R. A. Vincent (1995), Gravity wave activity in the lower atmosphere: Seasonal and latitudinal variations, *J. Geophys. Res., 100*, 1327-1350.

Bittner, M., D. Offermann, and H. U. Widdel (1997), Nonlinear resonant interaction of atmospheric gravity waves derived from chaff-wind data: a case study, Proceedings 13th ESA Symposium on European Rocket and Balloon Programmes and Related Research, Öland, Sweden, 26-29 May 1997, ESA SP-397, pp 489-494.

Borsche, M., G. Kirchengast, and U. Foelsche (2007), Tropical tropopause climatology as observed with radio occultation measurements from CHAMP compared to ECMWF and NCEP analyses, *Geophys. Res. Lett., 34*, L03702, doi:10.1029/2006GL027918.

Bühler, O. and M. E.McIntyre (2003), Remote recoil: a new wave-mean interaction effect, *J. Fluid Mech., 492*, 207-230.

Burrage, M.D., R.A. Vincent, H.G. Mayr, W.R. Skinner, N.F. Arnold and P.B. Hays (1996), Long-term variability in the equatorial middle atmosphere zonal wind, *J. Geophys. Res., 101*, 12,847-12,854.

Charron M., E. Manzini, and C. D. Warner (2002), Intercomparison of gravity wave parameterizations: Hines Doppler-spread and Warner and McIntyre ultra-simple schemes, *J. Met. Soc. Japan, 80*, 335-345.

Chimonas, G. (1999), Reply to comments on "Waves and the middle atmosphere wind irregularities", *J. Atmos. Sci., 39*, 2,041-2,042.

de la Torre, A., T. Schmidt and J. Wickert (2006), A global analysis of wave potential energy in the lower and middle atmosphere from CHAMP and SAC-C GPS-RO long term data, Geophys. Res. Lett., 33, L24809, doi:10.1029/2006GL027696.

Dörnbrack, A. and M. Leutbecher (2001), Relevance of mountain wave cooling for the formation of polar stratospheric clouds over Scandinavia: A 20 year climatology, *J. Geophys. Res., 106*, 1583-1593.

Dunkerton, T.J. (1997), The role of gravity waves in the quasi-biennial oscillation, *J. Geophys. Res., 102*, 26,053-26,076.

Eckermann, S. D., I. Hirota, and W K. Hocking (1995), Gravity wave and equatorial wave morphology of the stratosphere derived from long-term rocket soundings, *Quart. J. Roy. Met. Soc., 121*, 146-186.

Eckermann, S. D. and C. J. Marks (1997), GROGRAT: a New Model of the Global Propagation and Dissipation of Atmospheric Gravity Waves, *Adv. Space Res., 20*, 1253-1256.

Eckermann, S.D. and P. Preusse (1999), Global Measurements of Stratospheric Mountain Waves from Space. *Science, 286*, 1534-1537.

Eckermann S. D. and D. L. Wu (2006), Imaging gravity waves in lower stratospheric AMSU-A radiances, Part 1: simple forward model *Atmos. Chem. Phys., 6*, 3325-3341.

Eckermann, S. D., D. L. Wu, J. D. Doyle, J. F. Burris, T. J. McGee, C. A. Hostetler, L. Coy, B. N. Lawrence, A. Stephens, J. P. McCormack, and T. F. Hogan (2006), Imaging gravity waves in lower stratospheric AMSU-A radiances, Part 2: validation case study, *Atmos. Chem. Phys., 6*, 3343-3362.

Ern, M., P. Preusse, M.J. Alexander, and C.D. Warner (2004), Absolute values of gravity wave momentum flux derived from satellite data. *J. Geophys. Res., 109*, D20103, doi:10.1029/2004JD004752.

Ern, M., P. Preusse, and C.D. Warner (2006), Some experimental constraints for spectral parameters used in the Warner and McIntyre parameterization scheme, *Atmos. Chem. Phys., 6*, 4361-4381, 2006.

Ern, M., P. Preusse, M. Krebsbach, M. G. Mlynczak, and J. M. Russell III (2007), Equatorial wave analysis from SABER and ECMWF temperatures, *Atmos. Chem. Phys. Discuss., 7,* 11,685-11,723.

Fetzer, E. J., and J. C. Gille (1994), Gravity wave variances in LIMS temperatures, I, Variability and comparison with background winds, *J. Atmos. Sci., 51,* 2461-2483.

Fritts, D.C. (1984), Gravity Wave Saturation in the Middle Atmosphere: A Review of Theory and Observations, *Rev. Geophys., 22*, 275-308.

Fritts, D.C. and Alexander, M.J. (2003), Gravity wave dynamics and effects in the middle atmosphere. *Rev. Geophys. 41*, art. no. 1003.

Grossmann, K. U., D. Offermann, O. Gusev, J. Oberheide, M. Riese, and R. Spang (2002), The CRISTA-2 Mission, *J. Geophys. Res., 107*, 8173, doi:10.1029/2001JD000667.

Hagan, M. E., J. M. Forbes, and F. Vial (1995), On Modeling Migrating Solar Tides, *Geophys. Res. Lett. 22*, 893-896.

Hines, C. O. (1997), Doppler-spread parameterization of gravity-wave momentum deposition in the middle atmosphere. Part1: Basic formulation, *J. Atmos. Solar-Terr. Phys., 59*, 371-386.

Hines, C. O. (1999), Comments on "Waves and the middle atmosphere wind irregularities", *J. Atmos. Sci., 39*, 2,038-2,040.

Hirota, I. (1978), Equatorial waves in upper stratosphere and mesosphere in relation to semiannual oscillation of zonal wind, *J. Atmos. Sci., 35*, 714-722.

Jiang, J. H., D. L. Wu, and S. D. Eckermann (2002), Upper Atmosphere Research Satellite (UARS) MLS observations of mountain waves over the Andes, *J. Geophys. Res., 107*, 8273, doi:10.1029/2002JD002091.

Jiang, J. H., B. Wang, K. Goya, K. Hocke, S. D. Eckermann, J. Ma, D. L. Wu, and W. J. Read (2004a), Geographical distribution and interseasonal variability of tropical deep convection: UARS MLS observations and analyses, *J. Geophys. Res., 109*, D03111, 10.1029/2003JD003756.

Jiang, J. H., S. D. Eckermann, D. L. Wu, and J. Ma (2004b), A search for mountain waves in MLS stratospheric limb radiances from the winter Northern Hemisphere: Data analysis and global mountain wave modeling, *J. Geophys. Res. 109*, D03107, doi:10.1029/2003JD003974.

Kim Y. J., S. D. Eckermann, and H.-Y. Chun (2003), An overview of the past, present and future of gravity-wave drag parametrization for numerical climate and weather prediction models - Survey article, *Atmosphere-Ocean, 41*, 65-98.

Krebsbach, M. and P. Preusse (2007), Comparison of global distributions of zonal-mean gravity wave variance inferred from different satellite measurements, *Geophys. Res. Lett., 34*, L03814, doi:10.1029/2006GL028040.

Kutepov, A. A., A. G. Feofilov, B. T. Marshall, L. L. Gordley, W. D. Pesnell, R. A. Goldberg, and J. M. Russell III (2006), SABER temperature observations in the summer polar mesosphere and lower thermosphere: Importance of accounting for the CO2 $\nu 2$ quanta V-V exchange, *Geophys. Res. Lett., 33*, L21809, doi:10.1029/2006GL026591.

Manzini, E., and N.A. McFarlane (1998), The effect of varying the source spectrum of a gravity wave parameterization in a middle atmosphere general circulation model, *J. Geophys. Res., 103*, 31,523-31,539.

Marks, C. J., and S. D. Eckermann (1995), A Three-Dimensional Nonhydrostatic Ray-Tracing Model for Gravity Waves: Formulation and Preliminary Results for the Middle Atmosphere, *J. Atmos. Sci., 52*, 1959-1984.

McLandress, C. (1998), On the importance of gravity waves in the middle atmosphere and their parameterization in general circulation models, *J. Atmos. Sol.-Terr. Phys., 60*, 1357-1383.

McLandress, C., M. J. Alexander and D. L. Wu (2000), Microwave Limb Sounder observations of gravity waves in the stratosphere: a climatology and interpretation, *J. Geophys. Res., 105*, 11,947-11,967.

McLandress C. and J. F. Scinocca (2005), The GCM response to current parameterizations of nonorographic gravity wave drag, *J. Atmos. Sci., 62*, 2394-2413.

Medvedev A. S. and G. P. Klaassen (2000), Parameterization of gravity wave momentum deposition based on nonlinear wave interactions: basic formulation and sensitivity tests, *J. Atmos. Sol.-Terr. Phys., 62*, 1015-1033.

Mertens, C. J., M. G. Mlynczak, M. Lpez-Puertas, P. P. Wintersteiner, R. H. Picard, J. R. Winick, L. L. Gordley, and J. M. Russell III (2001), Retrieval of mesospheric and lower thermospheric kinetic temperature from measurements of CO_2 15 μm earth limb emission under non-LTE conditions, *Geophys. Res. Lett., 28*, 1391-1394.

Mertens, C. J., F. J. Schmidlin, R. A. Goldberg, E. E. Remsberg, W. D. Pesnell, J. M. Russel III, M. G. Mlynczak, M. Lopez-Puertas, P. P. Wintersteiner, R. H. Picard, J. R. Winick, and L. L. Gordley (2004), SABER observations of mesospheric temperatures and comparisons with falling sphere measurements taken during the 2002 summer MaCWAVE campaign, *Geophys. Res. Lett., 31*, L03105, doi:10.1029/2003GL018605.

Mlynczak, M.G. (1997), Energetics of the mesosphere and lower thermosphere and the SABER experiment, *Adv. Space Res. 20 (6)*, 1177-1183.

Oberheide, J., Q. Wu, T. L. Killeen, M. E. Hagan, and R. G. Roble (2006), Diurnal nonmigrating tides from TIDI wind data: Monthly climatologies and seasonal variations, *J. Geophys. Res., 111*, A10S03, doi:10.1029/2005JA011491.

Offermann, D., K. U. Grossmann, P. Barthol, P. Knieling, M. Riese, and R. Trant (1999), The CRyogenic Infrared Spectrometers and Telescopes for the Atmosphere (CRISTA) experiment and middle atmosphere variabilitiy, *J. Geophys. Res., 104*, 16,311-16,325.

Preusse, P., S. D. Eckermann, and D. Offermann (2000), Comparison of global distributions of zonal-mean gravity wave variance inferred from different satellite measurements, *Geophys. Res. Lett., 27*, 3877-3880.

Preusse, P., G. Eidmann, S. D. Eckermann, B. Schaeler, R. Spang and D. Offermann (2001), Indications of convectively generated gravity waves in CRISTA temperatures, *Adv. Space Res., 27*, 1653-1658.

Preusse, P., A. Dörnbrack, S. D. Eckermann, M. Riese, B. Schaeler, J. Bacmeister, D. Broutman, and K. U. Grossmann (2002), Space based measurements of stratospheric mountain waves by CRISTA, 1. Sensitivity, analysis method and a case study, *J. Geophys. Res., 107*(D23), 8178, doi:10.1029/2001JD000699.

Preusse, P. and M. Ern (2005), Indication of convectively generated gravity waves observed by CLAES, *Adv. Space Res., 35*, doi:10.1016/j.asr.2004.09.005, 1987-1991.

Preusse P., M. Ern, S. D. Eckermann, C. D. Warner, R. H. Picard, P. Knieleing, M. Krebsbach, J. M. Russel III, M. G. Mlynczak, C. J. Mertens, and M. Riese (2006), Tropopause to mesopause gravity waves in August: measurement and modeling, *J. Solar-Terr. Phys., 68*, 1730-1751.

Preusse P., S. D. Eckermann, and M. Ern (2008), Transparency of the atmosphere to short horizontal wavelength gravity waves, *J. Geophys. Res.*, submitted.

Riese, M., R. Spang, P. Preusse, M. Ern, M. Jarisch, D. Offermann, and K. U. Grossmann (1999), Cryogenic Infrared Spectrometers and Telescopes for the Atmosphere (CRISTA) data processing and atmospheric temperature and trace gas retrieval, *J. Geophys. Res., 104*, 16,349-16,367.

Riese, M., F. Friedl-Vallon, R. Spang, P. Preusse, C. Schiller, L. Hoffmann, P. Konopka, H. Oelhaf, T. von Clarmann, M. Höpfner (2005), GLObal limb Radiance Imager for the Atmosphere (GLORIA): scientific objectives, *Adv. Space Res.,*, 989-995.

Roble, R. G., and E. C. Ridley (1994), A thermosphere-ionosphere-mesosphere-electrodynamics general circulation model (time-GCM): Equinox solar cycle minimum simulations (30-500 km), Geophys. Res. Lett., 21, 417-420.

Russell, J.M. III, M.G. Mlynczak, L.L. Gordley, J. Tansock, and R. Esplin (1999), An overview of the SABER experiment and preliminary calibration results, *Proc. SPIE, 3756*, 277-288.

Song I.-S. and H.-Y. Chun, A lagrangian spectral parameterization of gravity wave drag induced by cumulus convection (2008), *J. Atmos. Sci.*

Tang J., G. R. Swenson, A. Z. Liu, F. Kamalabadi (2005), Observational investigations of gravity wave momentum flux with spectroscopic imaging, *J. Geophys. Res., 110*, D09S09, doi:10.1029/2004JD004778.

Tsuda, T., M. Nishida, C. Rocken and R. H. Ware (2000), A global morphology of gravity wave activity in the stratosphere revealed by the GPS Occultation data (GPS/MET) *J. Geophys. Res., 105*, 7,257-7,273.

Tsuda, T. and K. Hocke (2002), Vertical wave number spectrum of temperature fluctuations in the stratosphere using GPS occultation data, *J Met. Soc. Japan, 80*, 925-938.

Vadas S. L. and Fritts D.C (2002), The importance of spatial variability in the generation of secondary gravity waves from local body forces, *Geophys. Res. Lett., 29*, 10.1029/2002GL015574

Warner, C.D.,and M.E. McIntyre (1999), Toward an ultra-simple spectral gravity wave parameterization for general circulation models, *Earth Planets Space, 51*, 475-484.

Warner, C. D. and M. E. McIntyre, An ultra-simple spectral parameterization for non-orographic gravity waves, *J. Atmos. Sci., 58*, 1837-1857, 2001.

Wu, D. L. and J. W. Waters (1997), Observations of gravity waves with the UARS Microwave Limb Sounder, in *Gravity Wave Processes and Their Parametrization in Global Climate Models*, edited by K. Hamilton, Springer Verlag, New York.

Wu, D. L. and F. Zhang (2004), A study of mesoscale gravity waves over the North Atlantic with satellite observations and a mesoscale model, J. Geophys. Res, 109, D22104, doi:10.1029/2004JD005090.

Wu, D. L. (2006), Small-scale fluctuations and scintillations in high-resolution GPS/CHAMP SNR and phase data, *J. Atmos. Sol.-Terr. Phys., 68*, 999-1017.

Wu, D. L., P. Preusse, S. D. Eckermann, J. H. Jiang, M. de la Torre Juarez, L. Coy, B. Lawrence, and D. Y. Wang (2006), Remote sounding of atmospheric gravity waves with satellite limb and nadir techniques, *Adv. Space Res., 37*, 2269-2277.

Wüst S. and M. Bittner (2006), Non-linear resonant wave-wave interaction (triad): Case studies based on rocket data and first application to satellite data, *J. Atmos. Sol.Terr. Phys., 68*, 959-976.

Yee, J. H., E. R. Talaat, A. B. Christensen, T. L. Killeen, J. M. Russell, and T. N. Woods (2003), TIMED instruments, *Johns Hopkins APL Technical Digest 24 (2)*, 156-164.

Peter Preusse, Manfred Ern and Martin Riese, Institute of Chemistry and Dynamics of the Geosphere, ICG-1: Stratosphere, Research Center Juelich, Juelich, Germany. (p.preusse@fz-juelich.de)

S. D. Eckermann, Space Science Division, Code 7646, Naval Research Laboratory, Washington, DC 20375-5352, USA, (email stephen.eckermann@nrl.navy.mil)

Jens Oberheide, Department of Physics, Wuppertal University (BUGW), Gauss Str. 20, D-42097 Wuppertal, Germany

Richard H. Picard, Air Force Research Laboratory Battlespace Environment Division AFRL/VSBYB 29 Randolph Road Hanscom AFB, MA 01731-3010, USA

Ray Roble, High Altitude Observatory, NCAR, National Center for Atmospheric Research, 3450 Mitchell Lane, Boulder, CO 80307, USA

James M. Russell III, Department of Physics Hampton University Hampton, VA 23668, USA

Martin G. Mlynczak, NASA Langley Research Center Hampton, VA 23681-0001, USA

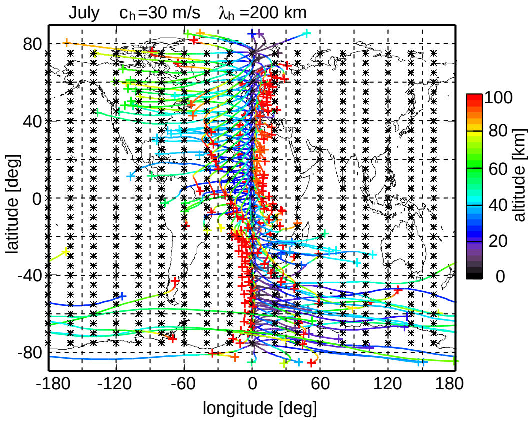

Figure 1. Launch distribution of one SCE (λ_h =200 km, c =30 ms^{-1}, $\hat{u}_{launch}$ =1 ms^{-1}). At each black asterisk eight rays are launched in eight different directions. Rays starting from 0° longitude are shown as an example. Color code gives altitude.

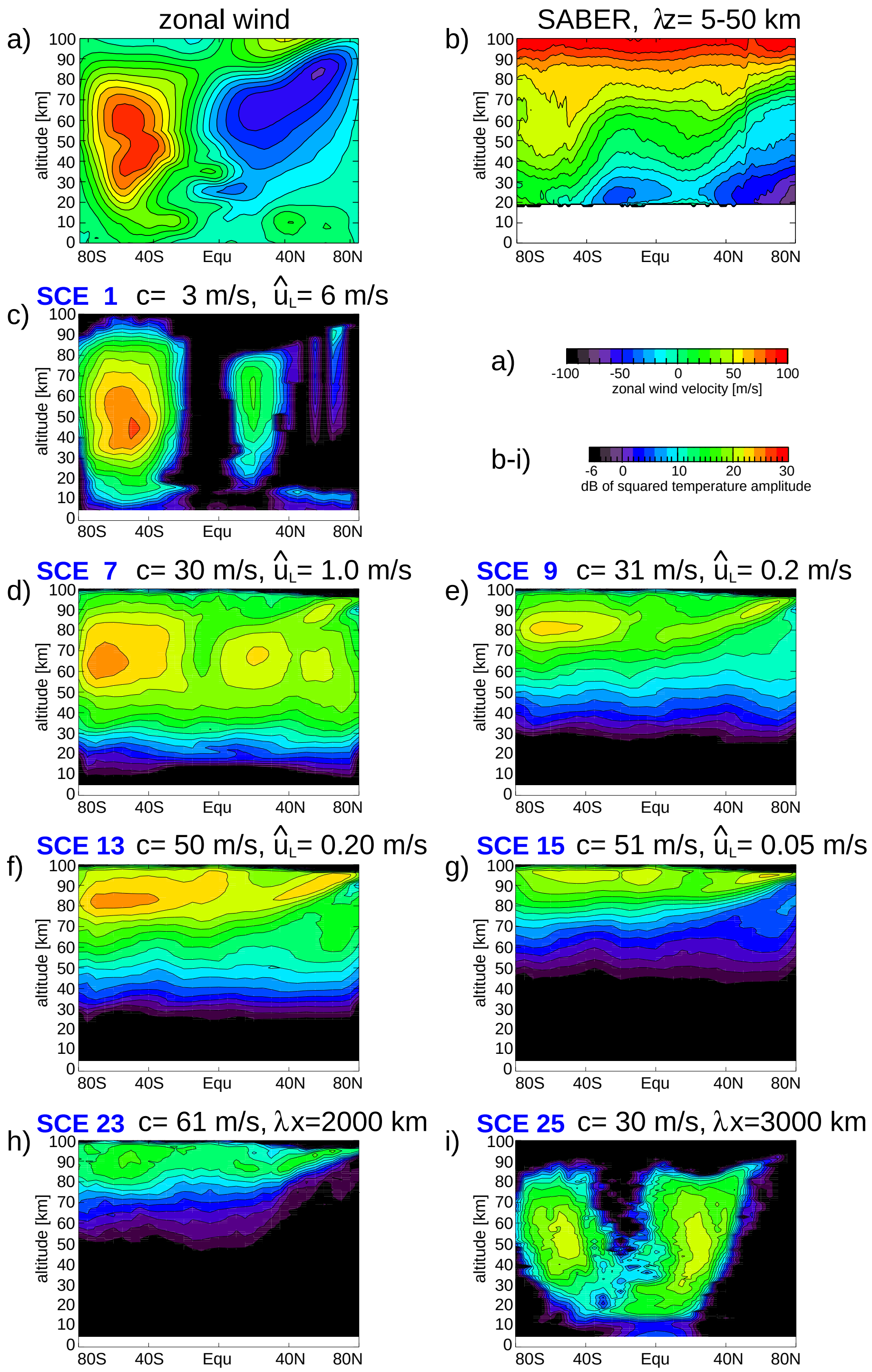

Figure 2. Comparison of SABER GW squared amplitudes with zonal mean winds and different GROGRAT SCEs as specified in Table 1. Panels c)-g) show mesoscale waves with 200 km horizontal wavelength. For details see text.

Table 1. Overview of the launch parameters for various SCEs. The panel is given for those SCEs shown in Figure 2. The different composites (Ex0, ... Ex232) shown in Figure 3 differ in the intermittency factor (IMF) attributed to the single SCEs in generating the composite.

SCE #	Fig.	λ_h [km]	c_h [ms^{-1}]	ampl. $\hat{u}_l$ [ms^{-1}]	Ex00 IMF	Ex04 IMF	Ex14 IMF	Ex32 IMF	Ex132 IMF	Ex232 IMF
BGRD				0.5 K	5.0	5.0	5	0	0	0
1	2c	200	3	6.00	1.0	1.0	10	20	0	0
2		500	3	6.00	0.0	0.0	0	0	20	20
3		200	10	20.00	0.4	0.4	10	5	0	0
4		500	10	20.00	0.0	0.0	0	0	5	5
5		200	20	2.00	0.0	0.0	5	5	0	0
6		500	20	2.00	0.0	0.0	0	0	5	5
7	2d	200	30	1.00	1.0	0.0	2	5	0	0
8		500	30	1.00	0.0	0.0	0	0	5	5
9	2e	200	31	0.20	0.0	1.0	10	10	10	0
10		500	31	0.20	0.0	0.0	0	0	0	10
11		200	40	0.10	0.0	0.0	10	20	20	0
12		500	40	0.10	0.0	0.0	0	0	0	20
13	2f	200	50	0.20	0.5	0.0	2	0	0	0
14		500	50	0.20	0.0	0.0	0	0	0	0
15	2g	200	51	0.05	0.0	0.5	30	50	50	0
16		500	51	0.05	0.0	0.0	0	0	0	50
17		200	90	0.05	0.0	0.0	0	60	60	0
18		500	90	0.05	0.0	0.0	0	0	0	60
19		2000	15	2.00	0.0	0.0	0	30	30	30
20		1000	30	1.00	0.0	0.0	0	0	0	0
21		1500	30	1.00	0.0	0.0	20	20	20	20
22		2000	60	0.20	0.0	0.0	30	20	20	20
23	2h	2000	61	0.05	0.0	0.0	40	60	60	60
24		2000	30	1.00	1.0	1.0	20	20	20	20
25	2i	3000	30	6.00	1.0	1.0	20	5	5	5
26		6000	30	30.00	2.0	1.0	40	0	0	0

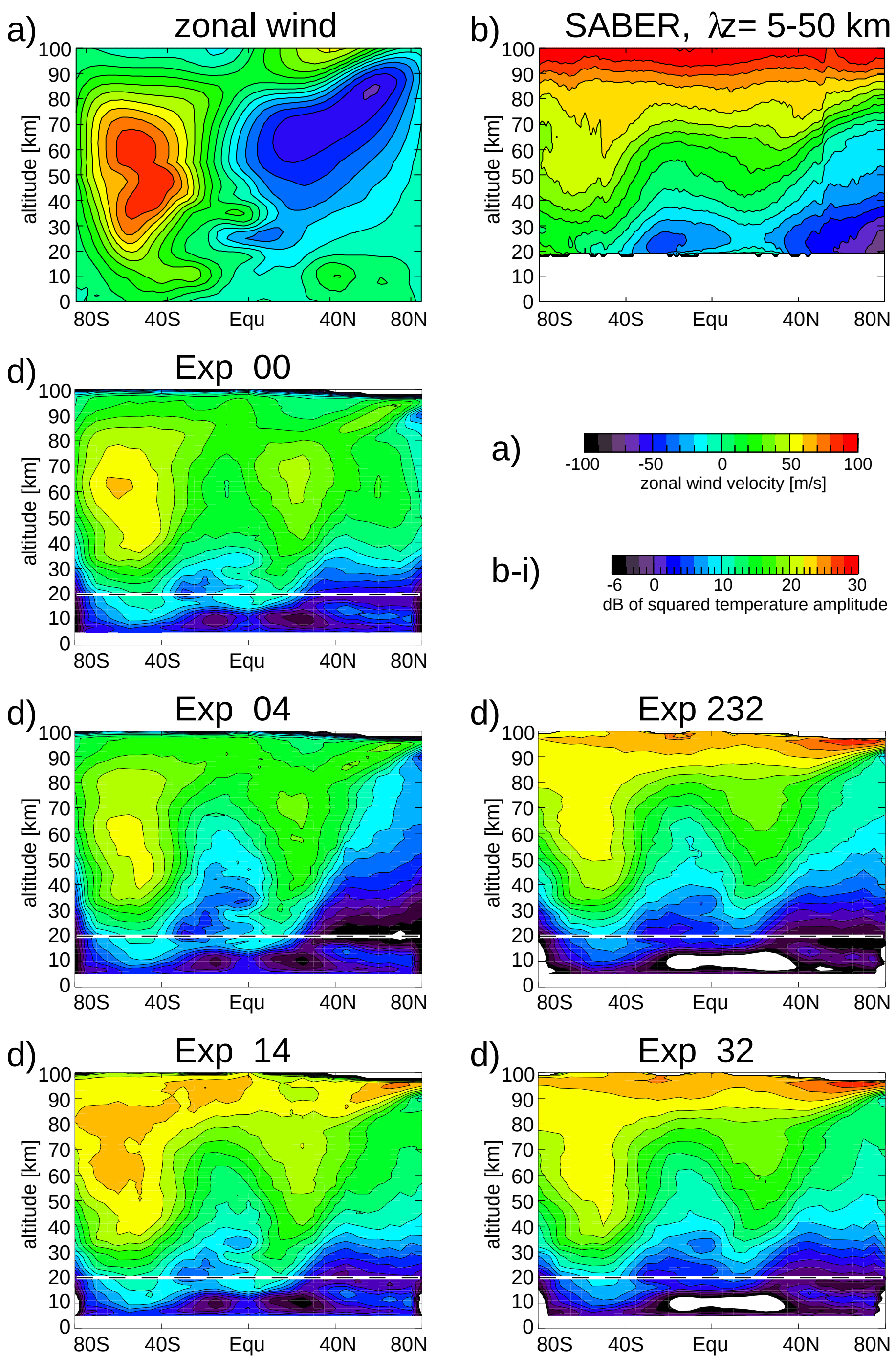

Figure 3. Comparison of SABER GW squared amplitudes with zonal mean zonal winds and different GROGRAT composite experiments. The composite experiments differ in the intermittency factors used to weight different SCEs (cf. Table 1). For details see text.

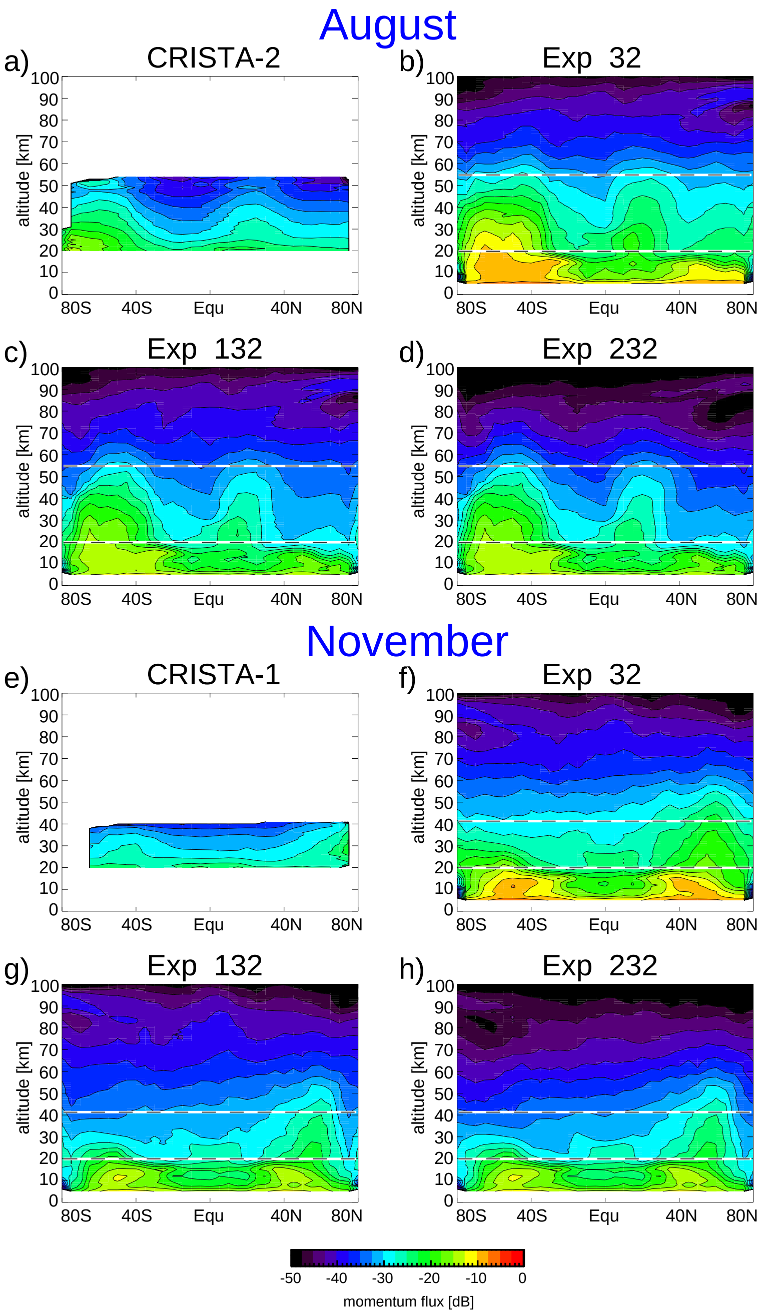

Figure 4. Comparison of measured absolute values of GW momentum flux by CRISTA-2 (Aug. 1997, panel a) and CRISTA-1 (Nov. 1994, panel e) with absolute values of momentum flux for composites 32 (b, f), 132 (c, g) and 232 (d, h) calculated for the 15 Aug. 2003 (b-d) and 15 Nov. 2003 (f-h). The difference between the three composites is the horizontal wavelength. Composite 32 uses λ_h =200 km for all mesoscale components, composite 132 λ_h =200 km for the fast waves and λ_h =500 km for the slow waves dominating the lower altitudes, and composite 232 uses λ_h =500 km for all mesoscale components. For discussion see text.

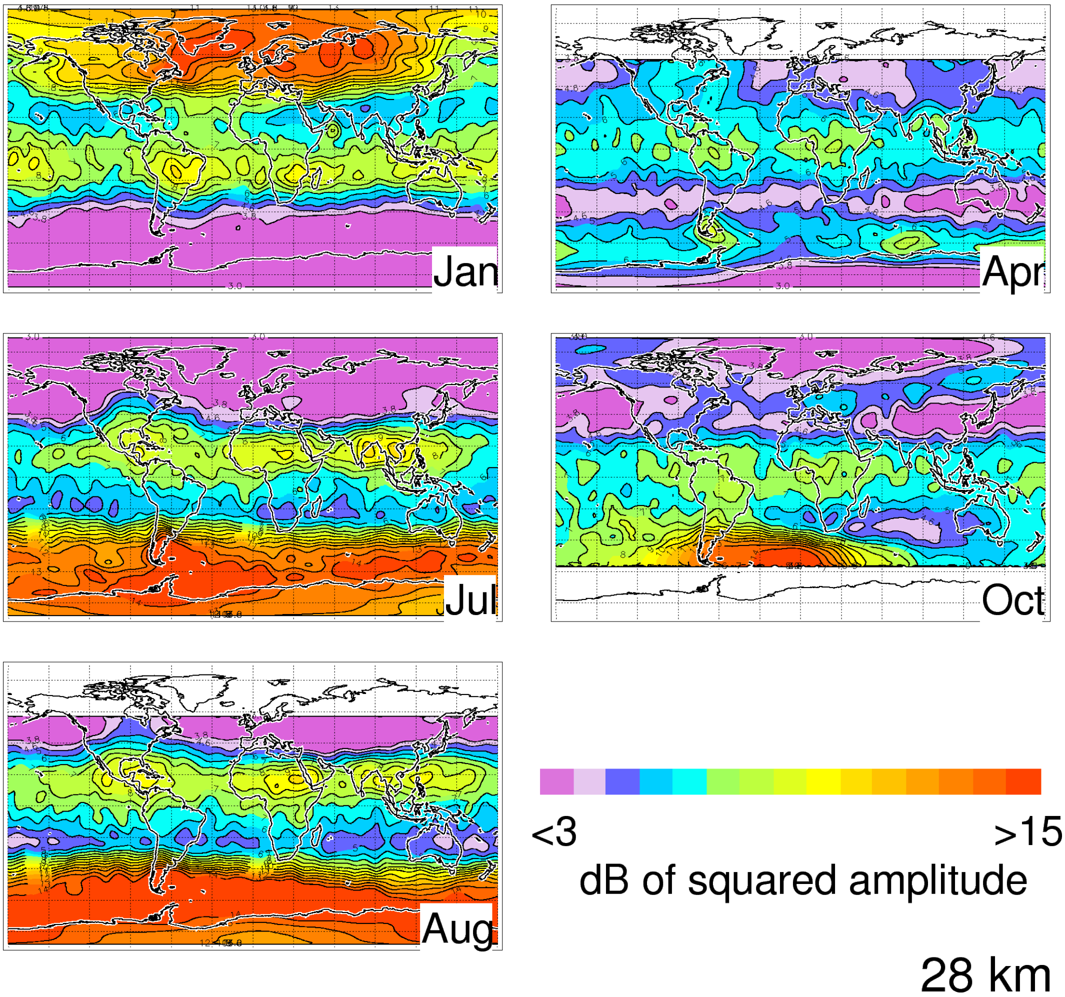

Figure 5. Global maps of SABER GW squared amplitudes for vertical wavelength from 5 km to 50 km at 28 km altitude. Values are binned according to calendar month for the time period from February 2002 to December 2006.

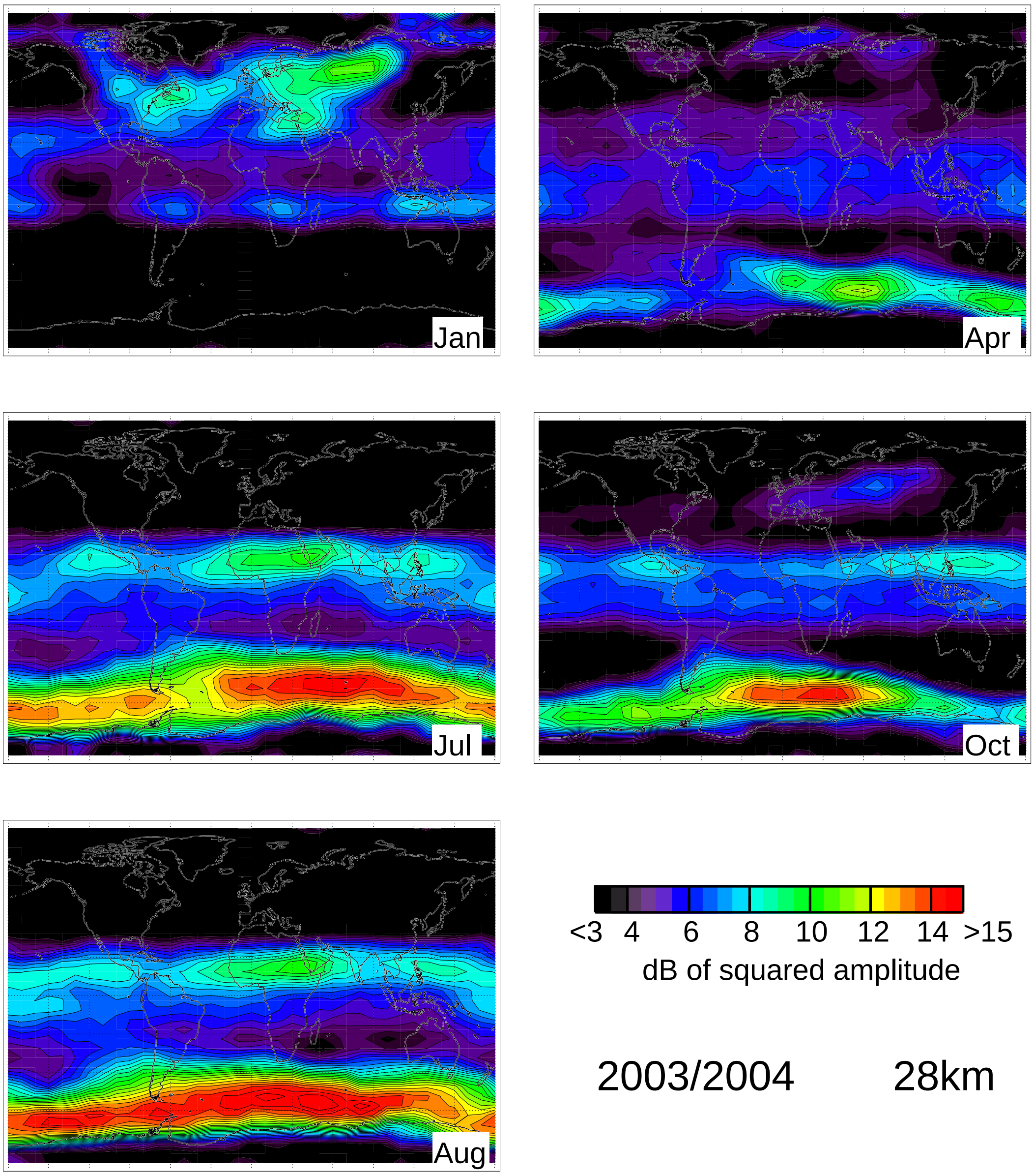

Figure 6. Global maps for 28 km altitude of GROGRAT GW squared temperature amplitudes from composite Exp232 for vertical wavelength from 5 km to 50 km. For details see text.

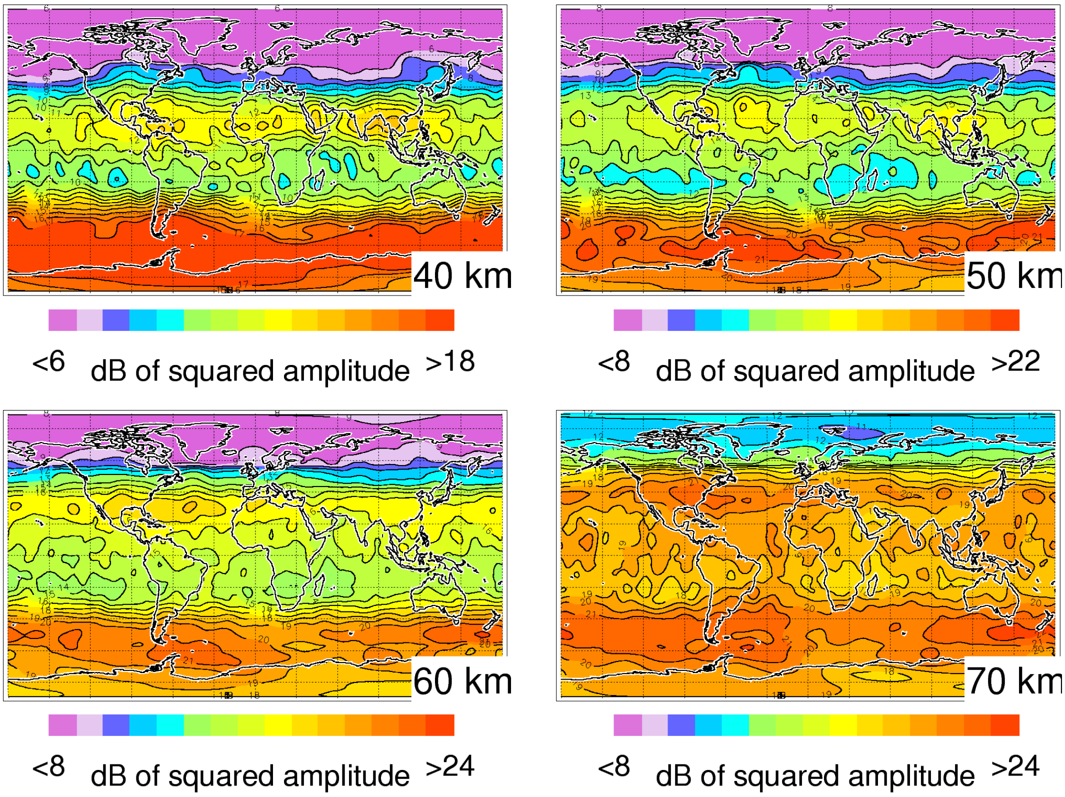

Figure 7. Same as Figure 5c, but for altitudes of 40, 50, 60, and 70 km

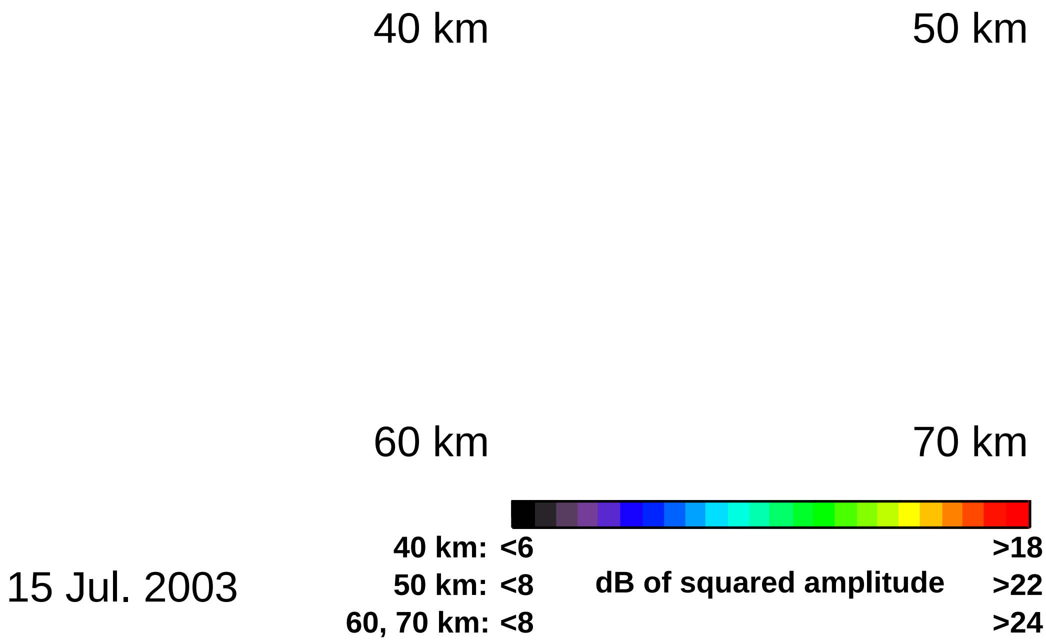

Figure 8. Same as Figure 6, but for July and altitudes of 40, 50, 60, and 70 km

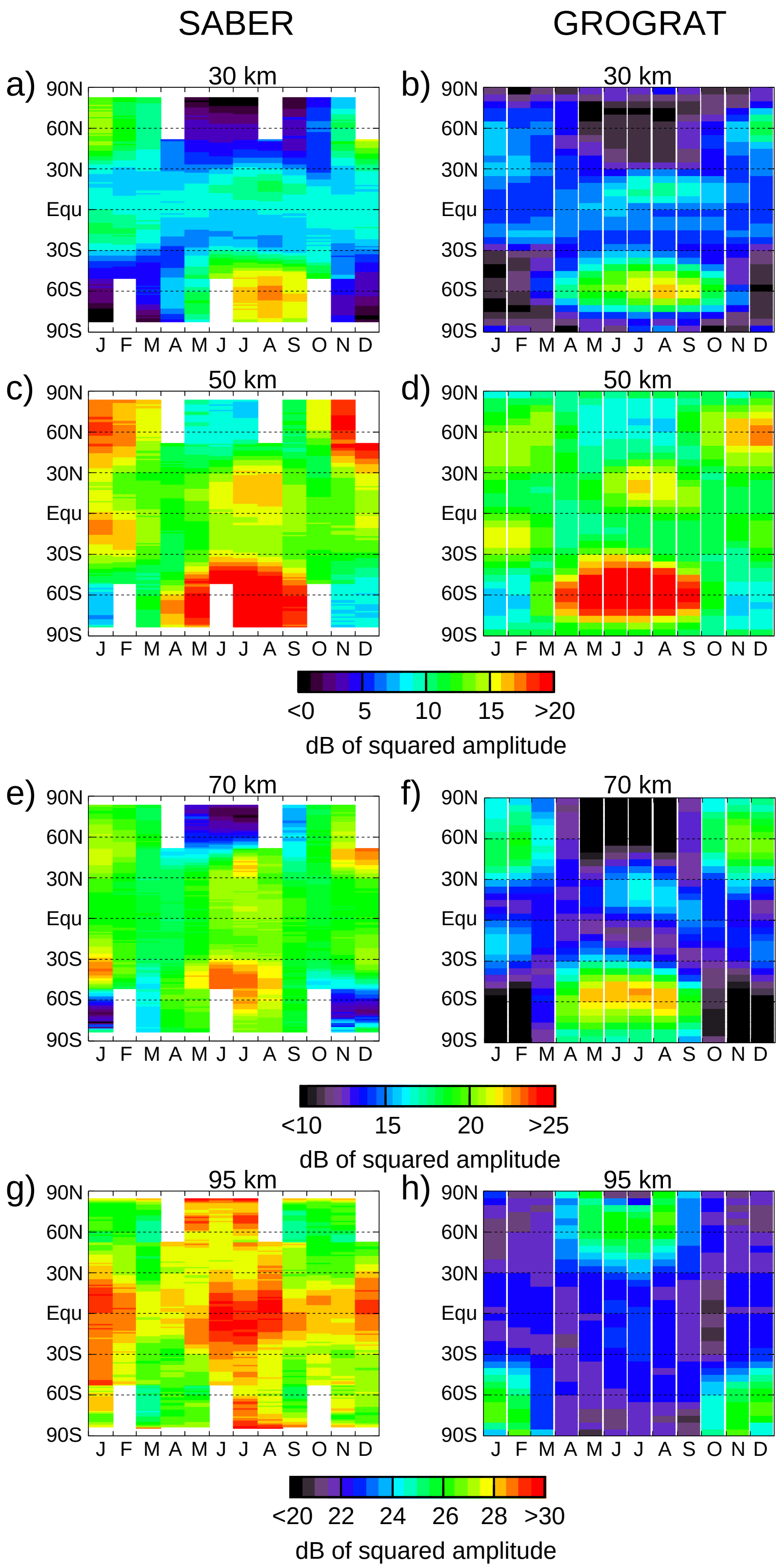

Figure 9. Time series of zonal mean GW squared amplitudes. SABER values (left column) are month averages, GROGRAT values from composite Exp232 (right column) are calculated for every third day of each month in 2003 and 2004. Color scales are the same for SABER and GROGRAT results for the respective altitudes of 30 km, 40 km, 70 km and 95 km. Most interesting, between 70 and 95 km altitude the wintertime maximum at lower altitudes reverses to a summertime maximum for mid and high latitudes.

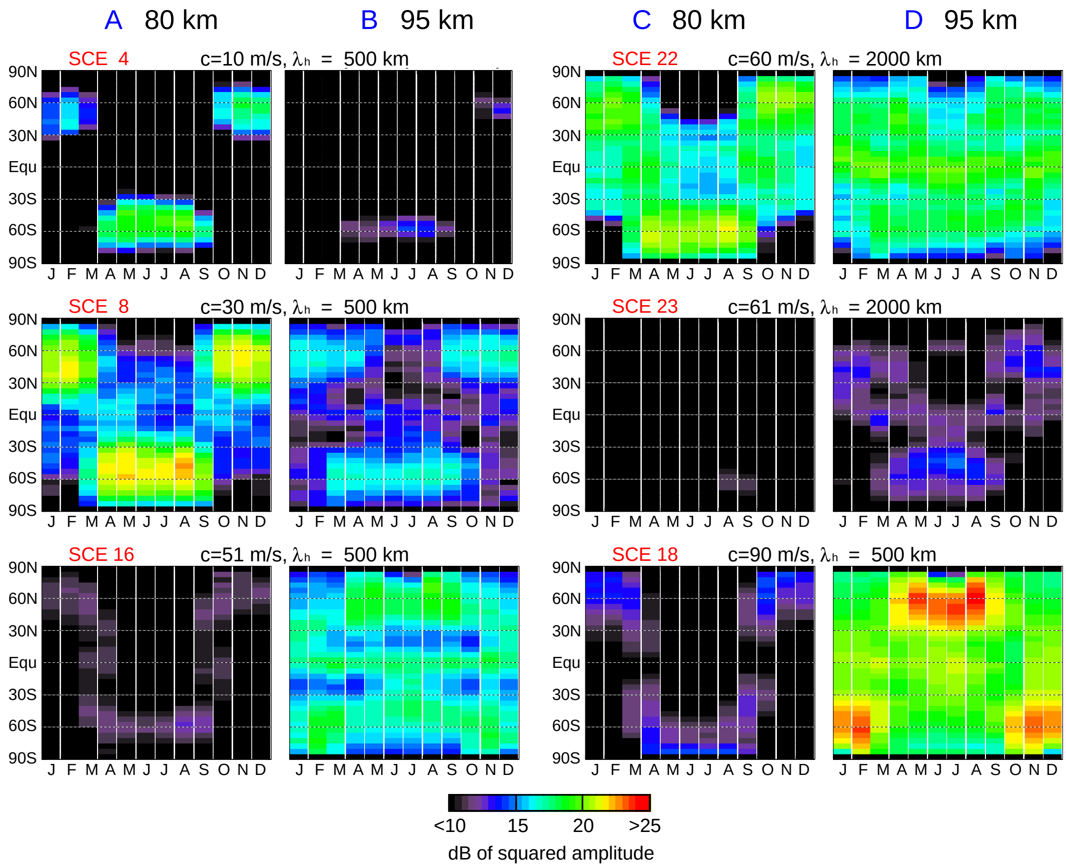

Figure 10. Time series of SCEs 4, 8, 16, 22, 23 and 18 at 80 km (columns A, C) and 95 km (columns B, D) altitude. The reversal from summer minimum to summer maximum between 80 and 95 km altitude is observed only in the fast mesoscale SCEs.

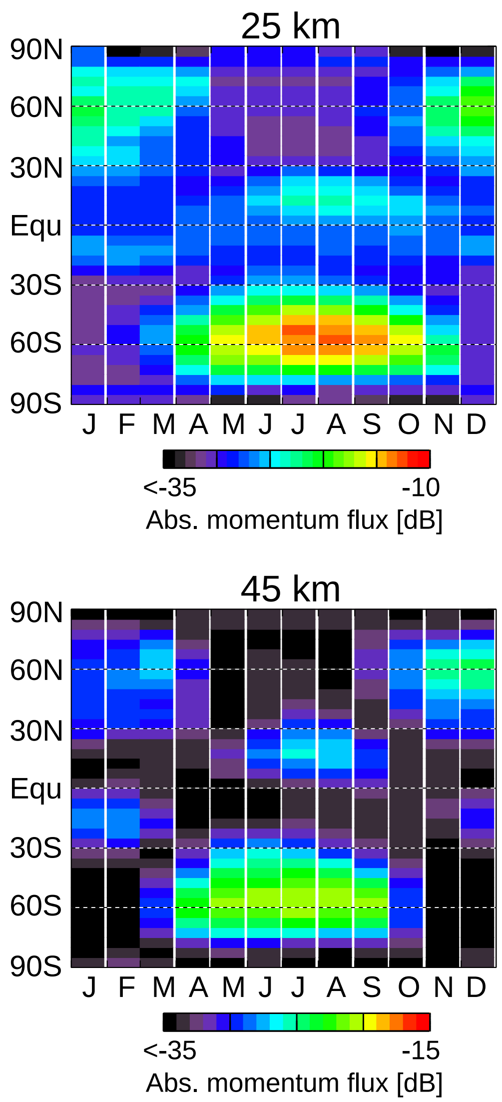

Figure 11. Time series of absolute values of GW momentum flux for experiment 232 at 25 and 45 km altitude. Waves with vertical wavelength $\lambda_z = [5, 25]$ km are shown.

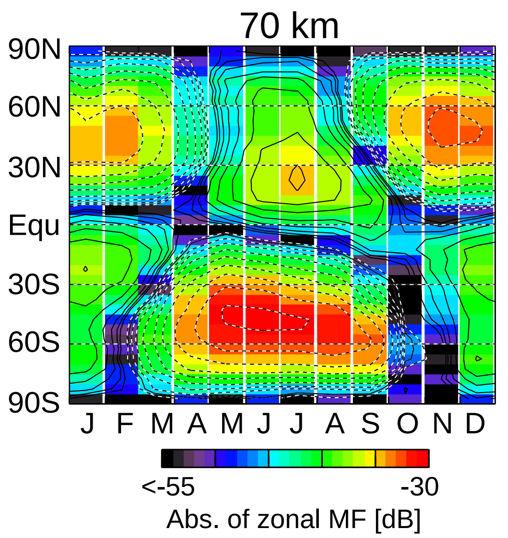

Figure 12. Time series of zonal momentum flux for composite 232 at 70 km altitude. Color code gives the absolute value of zonal GW momentum flux, contour lines show direction. Solid contours indicate positive values, i.e. preferentially eastward propagation, dashed contours negative values, i.e. preferentially westward propagation.

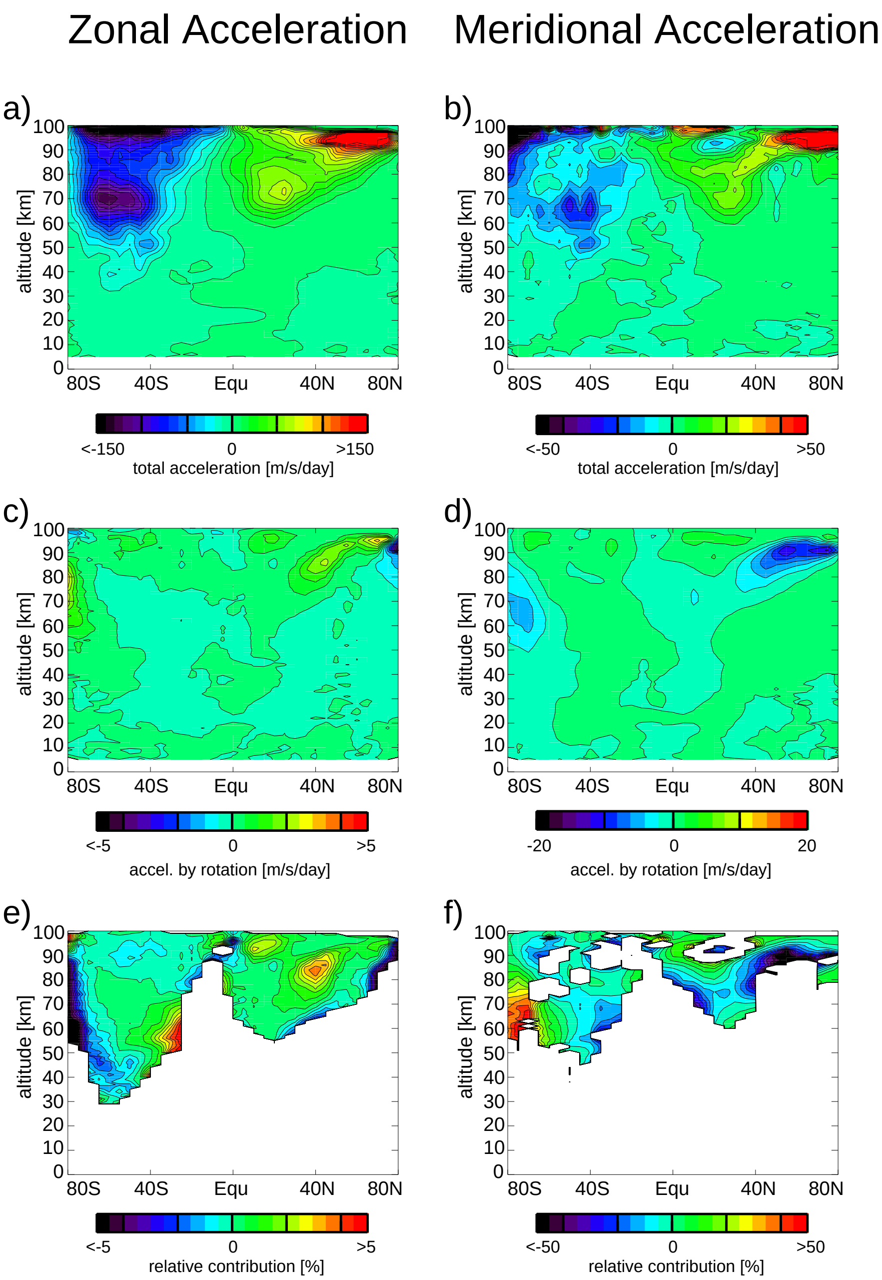

Figure 13. Zonal mean GW induced forcing. Left column shows zonal acceleration, right column shows meridional acceleration. The uppermost row gives the total values, the middle row the acceleration by turning of the wave vector due to GW refraction by horizontal wind gradients, and the lowermost row shows the relative contribution that is attributed to wave turning.

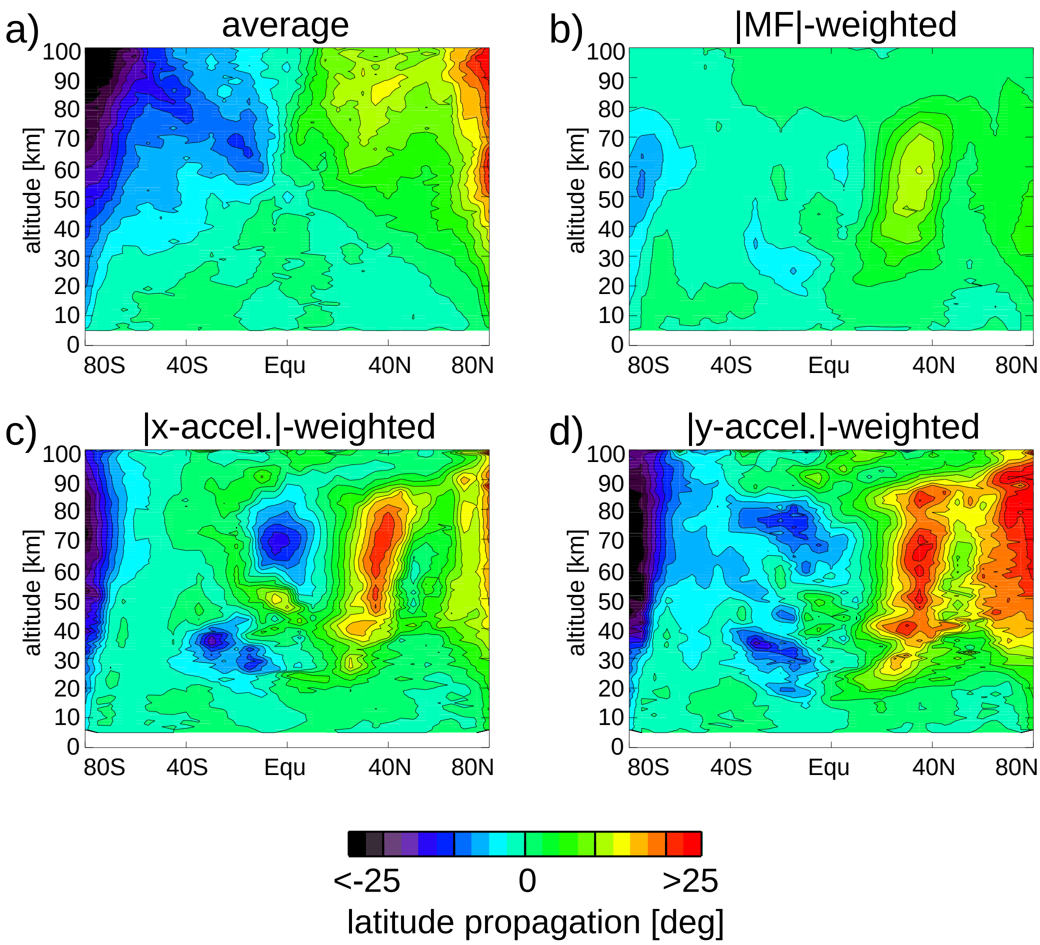

Figure 14. Zonal means of the latitude difference between the launch location and the point of observation (i.e. the altitude and latitude bin considered). Composite 232 for 15 July 2003 is shown. Panel a shows the average weighted only by the intermittency factors also used for the squared amplitudes and momentum flux values; panel b is additionally weighted by the absolute value of momentum flux of the individual waves; panel c and d are additionally weighted by the acceleration in the zonal and meridional direction.